Applied Ocean Research 97 (2020) 102071

Contents lists available at ScienceDirect

Applied Ocean Research

journal homepage: www.elsevier.com/locate/apor

CFD-based multi-objective optimisation of S60 Catamaran considering Demihull shape and separation

Aiqin Miao, Min Zhao, Decheng Wan*,†

Computational Marine Hydrodynamics Lab (CMHL), State Key Laboratory of Ocean Engineering, School of Naval Architecture, Ocean and Civil Engineering, Shanghai Jiao Tong University, Shanghai, 200240, China

ARTICLE INFO

Keywords:
CFD-based multi-objective optimisation
FFD method for NURBS surfaces
S60 catamaran
demihull shape and separation
OPTShip-SJTU solver
naoe-FOAM-SJTU solver

ABSTRACT

A computational fluid dynamics (CFD)-based multi-objective optimisation procedure is proposed for the development and application of the in-house solver OPTShip-SJTU. A free-form deformation (FFD) method is adopted to modify the non-uniform rational basis-spline (NURBS) surfaces of a ship and thus automatically reconstruct ship hull form. A Reynolds-averaged Navier–Stokes (RANS) solver, naoe-FOAM-SJTU, is applied to evaluate the hydrodynamic performance of a ship in the complex flow phenomena. The Non-Dominated Sorting Genetic Algorithm-II (NSGA-II) is used to search a global optimal set (called Pareto front) in approximation models constructed by the Kriging method. In this study, a S60 catamaran is optimised for resistance reduction based on a consideration of the demihull shape and separation. Three free-form deformation (FFD)-related parameters and the separation distance of the demihulls are selected as four design variables with two geometric constraints imposed. The total resistance for Froude numbers (F_r) = 0.4 and 0.45 are taken as the two objective functions. The optimal catamarans are obtained through an optimisation process and three of these are selected for further validation by a RANS-based method. The hydrodynamic performance of the initial and optimal catamarans is compared in terms of resistance, wave elevation, pressure distribution, cross flow, interference factors and longitudinal wave cuts, which confirms the reliability of the ship design optimisation.

1. Introduction

Catamarans have become one of the most rapidly growing high-performance ship classes in the past few decades due to their superior stability, speed, seakeeping and manoeuvrability. In addition to these advantages, resistance performance is one of the key hydrodynamic parameters of catamarans, and it must be considered early in the ship design stage. The proposed Energy Efficient Design Index (EEDI) encourages ship designers to optimise ship resistance performance to provide energy savings and emission reductions.

In recent years, ship design optimisation has become a hot topic in ship engineering fields [2,40,31,32,30,6,18,38,37,36,4]. The Simulation-Based Design (SBD) framework has been developed and applied to the hydrodynamic optimisation of ship hull form. SBD integrates computer-aided design (CAD) systems, computational fluid dynamics (CFD) techniques and optimisation algorithms. In general, SBD consists of three main modules: a ship-surface modification module, a hydrodynamic performance evaluation module and an optimisation module.

A ship-surface modification module is used to modify ship hull form locally and globally to yield new ship designs. It generally involves one of two methods: the first is based on ship-surface mesh points, and the second is based on non-uniform rational basis-spline (NURBS) surfaces. The ship-surface mesh points method involves deforming a hull surface represented by discretised meshes, thus avoiding the need for mesh regeneration for every new ship, and is easy to implement and time-efficient. The disadvantage of this method is that large deformations may generate distorted meshes.

The NURBS method involves deforming a hull form represented by NURBS surfaces [35,10], and it has rapidly become a standard method for the representation and design of ship hull form. There are two ways to move NURBS control points. One is to directly change the positions of NURBS control points or the weighting factor of NURBS surfaces. However, this may generate a large number of design variables. The other is to use additional deformation methods to move NURBS control points, such as free-form deformation (FFD) or radial basis function (RBF) methods, which can generate fewer design variables.

Once a new ship hull is produced, the hydrodynamic performance evaluation module is applied to calculate its performance. This module

* Corresponding author.
E-mail address: dcwan@sjtu.edu.cn (D. Wan).
† http://dcwan.sjtu.edu.cn/

https://doi.org/10.1016/j.apor.2020.102071
Received 4 May 2019; Received in revised form 22 January 2020; Accepted 23 January 2020

involves one of two methods. The first method is based on potential flow theory, and it has been widely used in ship design optimisation due to its rapidity in evaluating hydrodynamic performance, which is an advantage during the optimisation of preliminary ship design. The second method is based on viscous flow theory. It can accurately predict ship hydrodynamic performance qualities such as resistance, seakeeping and manoeuvrability and can capture flow-field information in detail. However, this method causes much more expensive computational cost and much more time-consuming. With the rapid development of CFD and high-performance computing (HPC), ship design optimisation based on CFD has become possible. Thus, many scholars have used this second method, which utilises advanced CFD, to validate the hydrodynamic performance of an optimal ship design [6,12,36].

During a ship design optimisation, the optimisation algorithm is used to search the optimal solution of objective functions in design space. Currently, the most widely used optimisation algorithms are the Single-Objective Genetic Algorithm (SOGA) [9], the Particle Swarm Optimisation (PSO) [16] and the Non-dominated Sorting Genetic Algorithm-II (NSGA-II) [29,5], amongst others.

The optimisation process involves the hydrodynamic performance evaluation of many new ships, which is time-consuming and computationally expensive. An approximation technique is thus used to approximate the relationship between ship modification parameters and hydrodynamic performance values. A minimal sufficient number of new sample ships are first selected using a scientific Design of Experiment (DOE) method, and their hydrodynamic performance is predicted by high-precision numerical simulations. Then, the approximation model (also called a surrogate model) can be constructed. In the iterative optimisation process, the approximation model is used to directly evaluate the hydrodynamic performance of new ships. Current widely used approximation models are response surface models (RSM) [17], Kriging models [26,27] and RBF [1].

Overall, SBD enables ship design optimisation to be an intelligent and integrative process, which greatly reduces the requirement for manual intervention.

Catamaran resistance is mainly related to the shape and separation of the demihulls in that the demihulls' shape directly affects the form resistance of catamaran, whereas the separation of the demihulls has a large effect on the flow field between them. The proximity of the two demihulls generates significant interference, which affects both wave-making and viscous resistance [28, 8]. Therefore, the shape and separation of demihulls should be considered simultaneously in the design optimisation of catamaran hull lines.

SBD-based research has been conducted only on the design optimisation of demihull shape for catamarans and other multihulls. Tahara et al. [32,30] carried out a single- and multi-objective ship design optimisation for the Delft catamaran, which was optimised only for the best demihull shape, with a focus on the difference between potential flow-based optimisation and viscous flow-based optimisation. Yang et al. [11] selected a TriSWACH vessel as the optimisation object in studies reported in 2015. First, only the shape of the centre hull was changed to reduce the wave-making resistance based on the potential flow method and without considering the viscous effect. Then, an optimal centre hull was adopted in the further optimisation for the side hulls. The position configuration and shape of the side hulls were optimised based on an integrated computational tool that comprised the potential flow tool and a Euler/RANS/Navier-Stokes-based advanced CFD tool. Two sets of side hulls that generated the minimum wave drag were selected. In addition, Chen et al. [3] optimised the demihull shape of a Delft catamaran to reduce the drag at a fixed width, i.e. the separation between demihulls was not considered.

The Computational Marine Hydrodynamics Lab (CMHL) of Shanghai Jiao Tong University (SJTU) has independently developed a ship design optimisation solver, OPTShip-SJTU, for SBD-based hydrodynamic performance optimisation. Thus far, the three main modules of ship design optimisation mentioned above have been implemented in this C++ language-based solver, and it has been successfully used to optimise several benchmark ship models, as described in the literature [20,36,22].

Previously, ship hull form was modified based on discretised ship meshes and the hydrodynamic performance was evaluated by the NMShip-SJTU solver based on potential flow theory [21,41]. In this study, the OPTShip-SJTU solver has been further developed to integrate a NURBS-based hull surface representation and modification module and a RANS-based high-fidelity hydrodynamic evaluation module named naoe-FOAM-SJTU [25,39,24,33,34]. Using this approach, a S60 catamaran is optimised to validate the developed optimisation tools. The total resistances for Froude numbers (F_r) = 0.4 and 0.45 are taken as objective functions and evaluated by the naoe-FOAM-SJTU solver. The NURBS surfaces of the demihull are deformed by an FFD method, and three modification parameters and demihull separation are defined as the four design variables. Kriging-based approximation models are constructed as the resistance evaluation tools for the optimisation process. The NSGA-II algorithm is used to search for the optimal results in the approximation models, and the optimal catamarans are obtained. Finally, the naoe-FOAM-SJTU solver is used to validate and verify the optimisation results.

2. Shape modification method

Modifying ship hull lines effectively is the first crucial step in ship design optimisation. An excellent ship modification method should follow these general guidelines: the modified ship hull should be kept as smooth as the initial ship, the number of ship modification parameters should be as small as possible, and the method should be as flexible as possible to allow a large design space.

2.1. NURBS-based ship hull representation

Currently, NURBS surfaces are industry-standard tools for the representation and design of geometry. They can use one common mathematical form for any geometric shape and are sufficiently flexible to enable the design of a large variety of shapes. They also control the curvature of hull surface better than traditional mesh-based representation methods. Generally, a ship hull surface is represented as several NURBS surfaces.

A p^{th}-degree in the u direction and q^{th}-degree in the v direction NURBS-surface is defined by Eqs. (1) and (2):

$$P(u,v)=\frac{\sum_{i=0}^{m}\sum_{j=0}^{n}\omega_{ij}P_{ij}N_{i,p}(u)N_{j,q}(v)}{\sum_{i=0}^{m}\sum_{j=0}^{n}\omega_{ij}N_{i,p}(u)N_{j,q}(v)}=\sum_{i=0}^{m}\sum_{j=0}^{n}P_{ij}R_{i,p;j,q}(u,v) \tag{1}$$

$$R_{i,p;j,q}(u,v)=\frac{\omega_{ij}N_{i,p}(u)N_{j,q}(v)}{\sum_{r=0}^{m}\sum_{s=0}^{n}\omega_{rs}N_{r,p}(u)N_{s,q}(v)} \tag{2}$$

where, P_{ij} is the location vector of the control points, ω_{ij} is the weight of the control points P_{ij}, u and v are the parametric nodes corresponding to the control points P_{ij} and $N_{i,p}(u)$, $N_{j,q}(v)$ are the B-spline basis functions of degree p and q in the u and v directions, respectively, which are defined by Eqs. (3) and (4):

$$\begin{cases}N_{i,0}(u)=\begin{cases}1, \text{ if} u_i\le u\le u_{i+1}\\ 0,\text{else}\end{cases}\\ N_{i,p}=\frac{u-u_i}{u_{i+p}-u_i}N_{i,p-1}+\frac{u_{i+p+1}-u}{u_{i+p+1}-u_{i+1}}N_{i+1,p-1}\end{cases} \tag{3}$$

$$\begin{cases}N_{j,0}(v)=\begin{cases}1, \text{ if} v_j\le v\le v_{j+1}\\ 0,\text{else}\end{cases}\\ N_{j,q}=\frac{v-v_j}{v_{j+p}-v_j}N_{j,q-1}+\frac{v_{j+q+1}-v}{v_{j+q+1}-v_{j+1}}N_{j+1,q-1}\end{cases} \tag{4}$$

These equations are based on the non-uniform knot vectors U={u_i}, V={v_i}, which can be given by Eqs. (5) and (6):

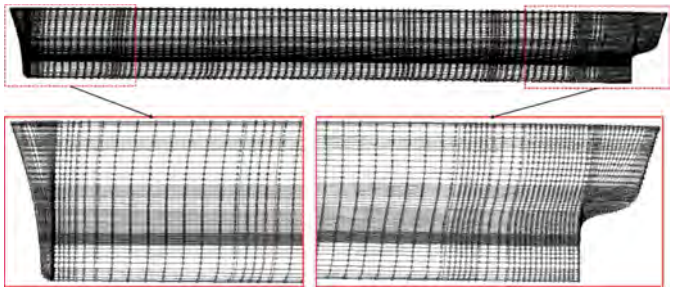

Fig. 1. A schematic diagram of NURBS control point distribution on a hull surface from the global (upper) and local (lower left: bow; lower right: stern) perspectives.

$$U = \left\{ \underbrace{a, \ldots, a}_{p+1}, u_{p+1}, \ldots, u_{m-p-1}, \underbrace{b, \ldots, b}_{p+1} \right\} \tag{5}$$

$$V = \left\{ \underbrace{c, \ldots, c}_{q+1}, v_{q+1}, \ldots, v_{n-q-1}, \underbrace{d, \ldots, d}_{q+1} \right\} \tag{6}$$

where, a, b, c, d are constants repeated with multiplicity of $p + 1$ and $q + 1$, which ensures the surface passes through the first and last control points and is tangent to the first and last sides. Internal knot values are unevenly spaced.

Fig. 1 shows the control points distribution of a ship represented by NURBS surfaces. It is better to manipulate the NURBS surfaces to refine the control points at the bow, stern and bilge, where the curvature of a ship changes greatly.

2.2. FFD method

The FFD method [23] is based on the elastic deformation of an elastic object. The object to be deformed is enveloped in a control lattice as shown in Fig. 2 and an external force is applied to the control lattice during deformation. Thus, all the surfaces of object within the lattice simultaneously undergo the same geometric deformation.

A local coordinate system $O' - STU$ is imposed on a parallelepipedal region, as shown in Fig. 2, where any point X (in the global coordinate system $O - XYZ$) has (s, t, u) coordinates in this system, such that

$$\mathrm{X} = \mathrm{X}_0 + s\mathrm{S} + t\mathrm{T} + u\mathrm{U} \tag{7}$$

The local coordinates can be computed using Eq. (8) as follows:

$$s = \frac{\mathrm{T} \times \mathrm{U}(\mathrm{X} - X_0)}{\mathrm{T} \times \mathrm{U} \cdot \mathrm{S}}, \quad t = \frac{\mathrm{S} \times \mathrm{U}(\mathrm{X} - X_0)}{\mathrm{S} \times \mathrm{U} \cdot \mathrm{T}}, \quad u = \frac{\mathrm{S} \times \mathrm{T}(\mathrm{X} - X_0)}{\mathrm{S} \times \mathrm{T} \cdot \mathrm{U}} \tag{8}$$

The objects to be deformed are completely enveloped by the parallelepiped; thus, it is obvious that $0 < s, t, u < 1$.

Next, the parallelepiped is cut into l, m and n parts along the S and T, U directions respectively, and a series of control nodes $P_{i,j,k}$ are generated on a lattice. In Fig. 2, $l = 5$, $m = 4$, $n = 4$, and the small black circles represent these control nodes, which have global coordinates that can be expressed according to Eq. (9):

$$P_{i,j,k} = X_0 + \frac{i}{l}\mathrm{S} + \frac{j}{m}\mathrm{T} + \frac{k}{n}\mathrm{U} i = 0, 1, \cdots l; \quad j = 0, 1, \cdots m; k = 0, 1, \cdots n \tag{9}$$

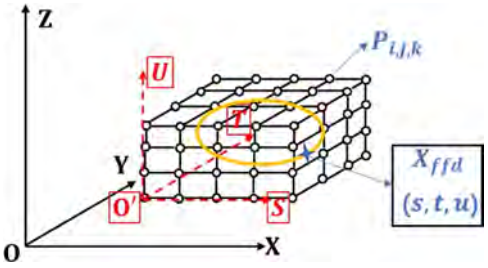

Fig. 2. A schematic diagram of FFD method.

Thus, the global coordinates of any point X with local coordinates (s, t, u) can be computed using the control nodes, as in Eq. (10):

$$\mathrm{X}(s, t, u) = \sum_{i=0}^{l} \sum_{j=0}^{m} \sum_{k=0}^{n} B_{i,j}(s) B_{j,m}(t) B_{k,n}(u) \mathbf{P}_{i,j,k} \tag{10}$$

where B represents a Bernstein polynomial, as defined by Eq. (11):

$$B_{i,n}(u) = \frac{n!}{i!(n-i)!} u^i (1-u)^{n-i} \tag{11}$$

The deformation is performed by moving the control nodes $P_{i,j,k}$ from their original lattice positions $P'_{i,j,k}$, and the deformed position X_{ffd} of any point X (s, t, u) can be obtained by Eq. (12):

$$\mathrm{X}_{ffd} = \sum_{i=0}^{l} \sum_{j=0}^{m} \sum_{k=0}^{n} B_{i,l}(s) B_{j,m}(t) B_{k,n}(u) \mathbf{P}'_{i,j,k} \tag{12}$$

where $\mathbf{P}'_{i,j,k}$ denotes the new locations of the control nodes in the global coordinate system.

The FFD method based on the NURBS geometric expression establishes the above relationship between the control nodes on the control lattice of the FFD method and the NURBS control points of the hull surface within the control lattice. When the FFD control nodes are moved, the new position of the NURBS control points can be obtained by Eq. (12), and then the new surface is obtained by the NURBS surface expression. The specific steps of this process are as follows (and depicted in Fig. 3): first, the parent ship NURBS file (generally, IGES file) is inputted to the OPTShip-SJTU solver. The control point coordinates on all NURBS surfaces are saved using the function readIGESWriteGO in the SINTEF SISL Library, which is the most mature and complete open source NURBS library currently available. Then, information on the FFD control lattice(s) and the movable FFD control nodes is inputted to the solver, and the local coordinates of all NURBS control points are calculated. Then, when the movable FFD control nodes change position, the new global coordinate of any NURBS control point, according to its local coordinate and the new global coordinates of all FFD control nodes, can be reobtained by use of Eq. (12). Finally, we use the SISL library function readGoWriteIGES to obtain the NURBS file for the new ship. The method is applied to a ship bow modification and the initial and deformed ships are shown in Figs. 4 and 5.

3. CFD-based simulation of a S60 catamaran

3.1. CFD: RANS solver naoe-FOAM-SJTU

In this study, the resistance performance of a catamaran is calculated by the solver naoe-FOAM-SJTU, which is used to solve typical hydrodynamic problems in ship and marine engineering fields. It was developed on the open source CFD platform OpenFOAM. The governing equations are unsteady two-phase flow-incompressible Reynolds-Averaged Navier-Stokes (RANS) equations. The k-ω shear stress transport (SST) model is used for turbulence closure and the volume of fluid (VOF) method is applied to capture the free surface elevation. The VOF method is based on the volume fraction of the i th fluid (α_i). This parameter represents the volume fraction occupied by the i^{th} fluid inside an arbitrary closed volume and it is determined according to an averaged continuity equation.

The computational domain is discretised by the finite volume method (FVM). The pressure-implicit split-operator (PISO) algorithm is used to determine the pressure-velocity coupling when solving governing equations. The 6-DOF module of the solver can predict various

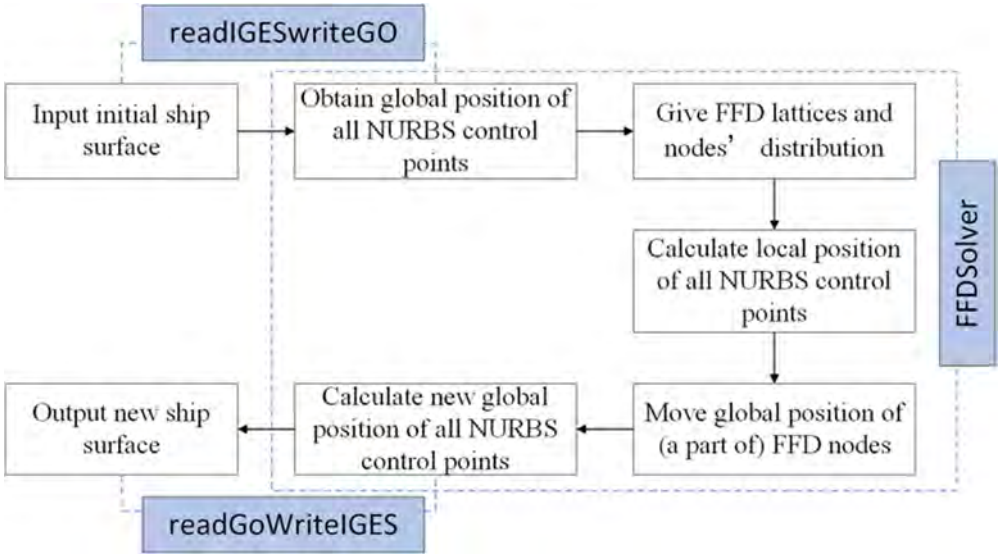

Fig. 3. Flow chart describing the FFD method based on the NURBS geometric expression for a ship hull.

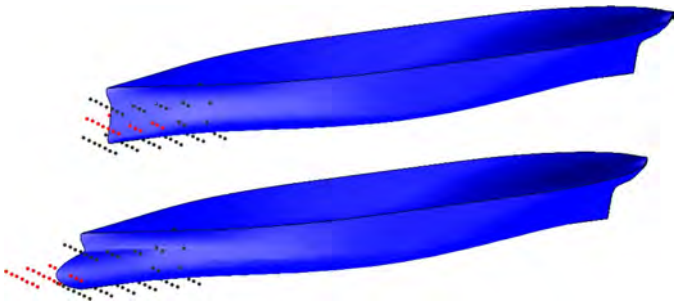

Fig. 4. FFD control nodes and the ship hull deformation under the FFD method based on the NURBS geometric expression for a ship hull (upper: before deformation; lower: after deformation).

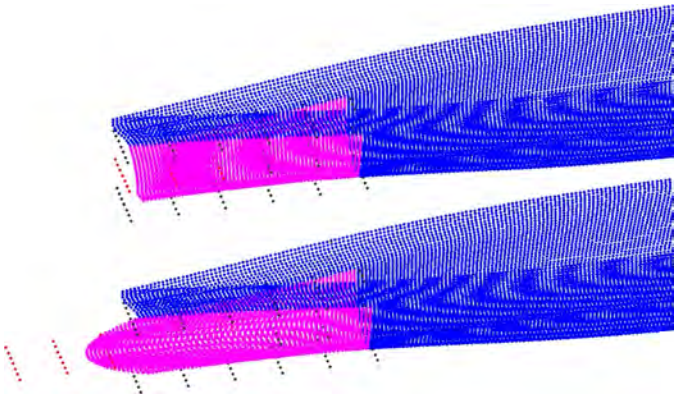

Fig. 5. FFD control nodes and the NURBS control points displacement of a ship hull under the FFD method, based on the NURBS geometric expression for a ship hull (upper: before deformation; lower: after deformation).

complex motions of ships. Many studies have verified the accuracy of the naoe-FOAM-SJTU solver for resistance prediction [25,33].

3.2. Computational model and calculation setup

To ensure the reliability of the subsequent ship design optimisation, we need to validate the accuracy of the numerical calculation of the ship's resistance performance. We thus first perform a numerical prediction of the resistance and flow field under different Fr for the mother ship S60 monohull and catamaran (only using C3 separation in the literature [28]: $s/L_{pp} = 0.3884$). The detailed geometrical properties of the S60 model are listed in Table 1. The geometry of the S60 catamaran configuration (S60_C3) can be seen in Fig. 6.

Table 1
The principal dimensions of the S60 monohull model.

Main particulars	Symbol	Value
Length between perpendiculars	L_{pp}/m	2.5
Beam	B/m	0.333
Draft	T/m	0.133
Wetted surface area	S_W/m^2	1.062
Displacement	Δ/m^3	0.0664

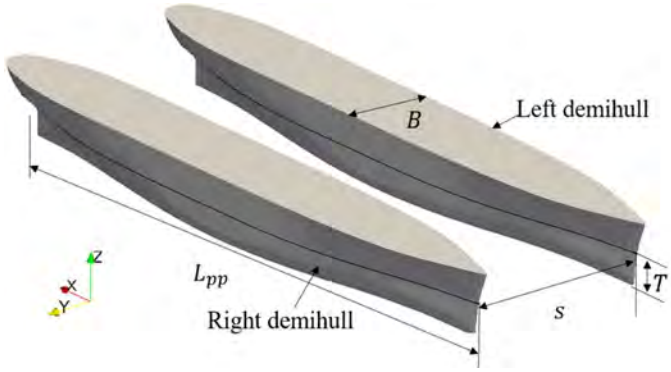

Fig. 6. The geometry of the S60_C3 catamaran configuration.

Given the fact that both the monohull and the catamaran are symmetrical along the mid-longitudinal section, only the right half of the computational domain is used, which greatly reduces the computational cost and time. The mesh generator snappyHexMesh in OpenFOAM is used for automatically generating meshes. The same size and grid refinement of the computational domain for both the monohull and the catamaran are carried out and shown in Figs. 7 and 8. Grids containing about 2.6 and 2.5 million cells are used for the monohull and the catamaran, respectively.

Boundary layers and boundary conditions are applied as shown in Figs. 9 and 10, which ensures that the y^+ value is more than 30.

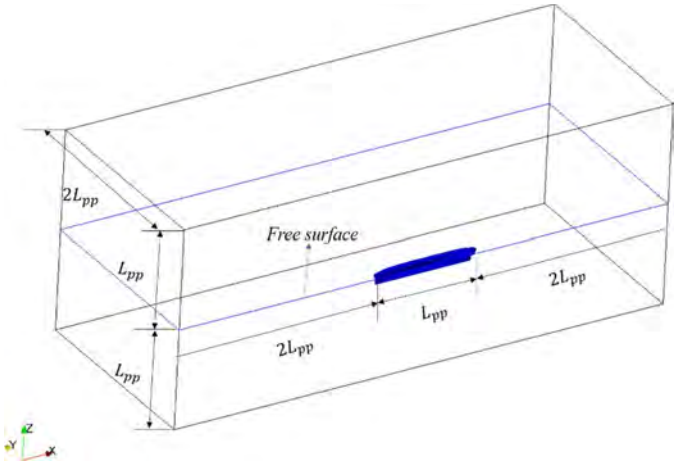

Fig. 7. The size of the computational domain.

3.3. Grid convergence study

Verification has been carried out for grid spacing. Convergence study is made according to ITTC procedure [13] for three solutions by three different meshes. Tables 2 and 3 show the numerical uncertainty results for the resistances of S60 monohull and S60_C3 catamaran model under different Fr. It turns out that the convergence condition is monotonic convergence from the values of R_G. As can be seen from the results of the grid convergence index, $GCI_{12} < GCI_{23}$ in all cases indicates that after reaching the medium mesh refinement, the numerical prediction results are less affected by the change of the grid. Therefore, all of the following numerical calculation are carried out under the medium mesh setup.

3.4. Numerical simulation results

Fig. 11 shows the results of the computations in towed conditions. Results are compared against previously reported experimental data

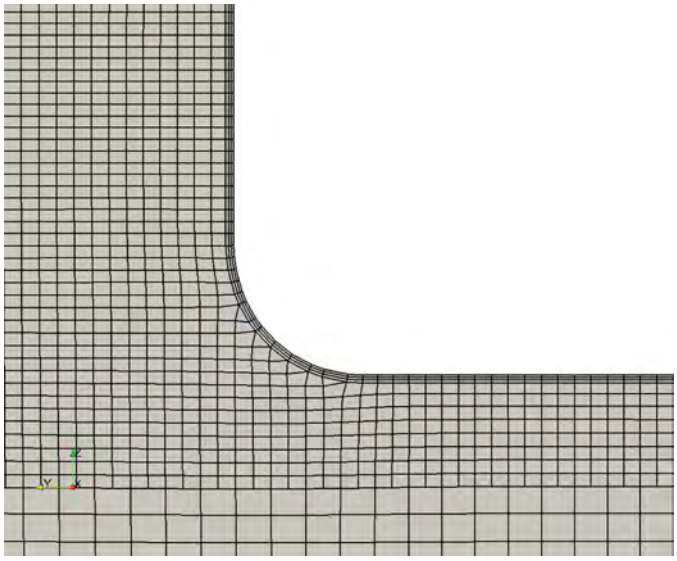

Fig. 9. The boundary layer of grids.

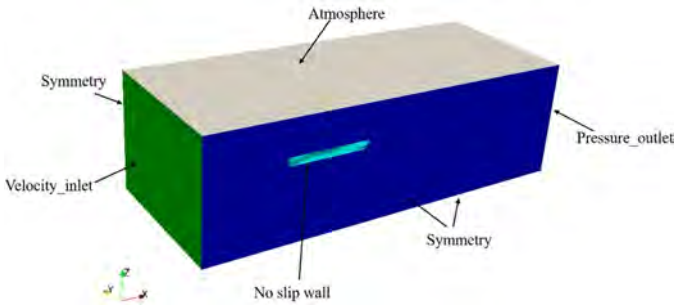

Fig. 10. Selected boundary conditions for the numerical simulation.

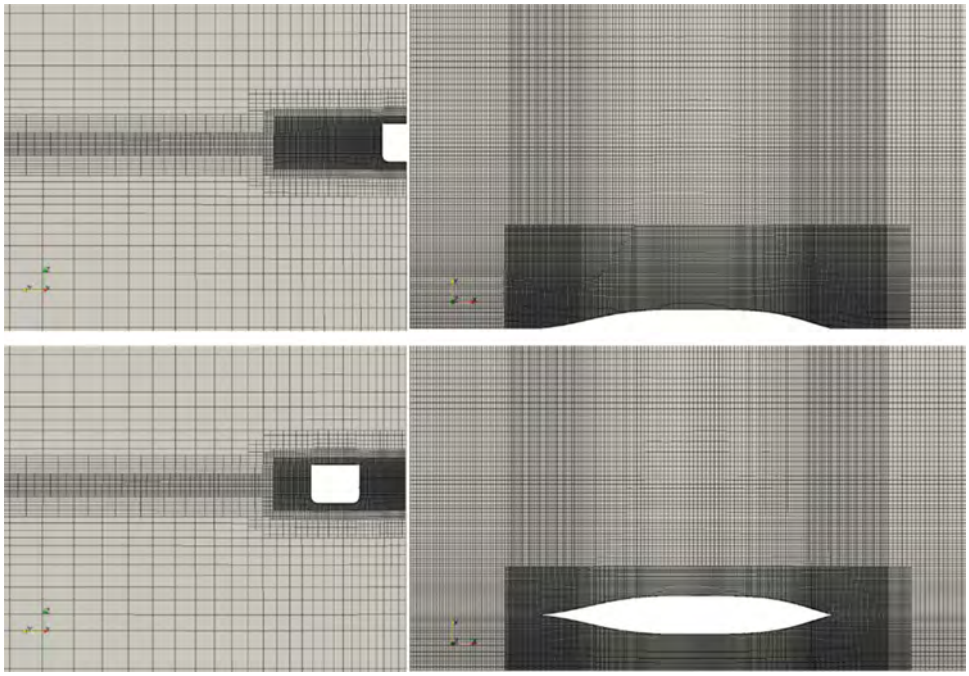

Fig. 8. The grids and refinements of the computational domain for the S60 monohull (upper) and S60_C3 catamaran models (lower).

Table 2
Grid convergence results for S60 monohull model.

Fr	R_t_EFD/N	r_G	R_G	$\varepsilon_{21}\%S_2$	$U_I\%S_2$	$U_G\%S_2$	$U_{SN}\%S_2$	GCI_{12}	GCI_{23}
0.30	5.744	1.414	0.484	0.506	0.078	0.538	0.543	0.598%	1.228%
0.35	8.643	1.414	0.613	0.823	0.080	2.270	2.272	1.646%	2.661%
0.40	17.089	1.414	0.592	0.775	0.048	1.817	1.818	1.414%	2.372%
0.45	27.282	1.414	0.457	0.905	0.043	1.051	1.052	0.959%	2.082%
0.50	36.375	1.414	0.535	0.763	0.054	1.111	1.112	1.108%	2.053%
0.55	43.890	1.414	0.578	1.139	0.045	2.392	2.392	1.969%	3.370%

[28]. The comparison of resistances shows excellent agreement between CFD and EFD. As can be seen from Fig. 11, numerical results are greater than the experimental results for the monohull for all F_r values. It is a pity that the experimental error is not given in the literature. But there is a possible reason. According to Farkas et al. [8], in experimental measurements, the total resistance values were measured in kilograms. For example, for $F_r = 0.3$, the resistance value amounts only 0.5855 kg. For such a small value, even small mistake or uncertainty can lead to relatively large deviation, 6.67%. For the catamaran S60_C3, the relative errors are much lower than that for the monohull for all F_r values except 0.55. However, for $F_r = 0.4$ and 0.45, the predictor error of S60_C3 resistance is within 3%, which is very small. It ensures the accuracy of numerical simulations for the next optimisation process.

4. Approximation model construction

Ship design optimisation requires many objective function evaluations. Suppose that the objective function is the total resistance of a ship and that the design variables are ship modification parameters. In the optimisation process, the total resistance of each new ship generated during every iteration needs to be evaluated. Generally, there is no certain mathematical expression linking the objective function and the design variables. If we use a viscous CFD numerical tool for every new ship, many computing resources and much time would be required, which may exceed those available to solve the engineering problem. An approximation technique can thus play an important role by replacing the expensive high-fidelity time-consuming CFD simulation in the optimisation process with an approximate model. In practice, the approximation technique involves a combination of statistical and mathematical methods to approximate the relationship between design variables and objective functions.

4.1. Sampling techniques

Sampling is required before an approximation model can be used. Reasonable sampling should fully express the design space with as few samples as possible, to improve the accuracy of the approximation model. In this study, the optimal Latin hypercube sample (OLHS) method, a modified Latin hypercube design, is used for sampling [36,20].

4.2. Kriging model

Kriging models are the most commonly used spatial interpolation algorithm and are widely used in geoscience, environmental science and atmospheric science research, amongst other fields. Therefore, we chose to use the Kriging model in this study. Kriging is a method that uses a regression algorithm to perform spatial modelling and prediction (interpolation) on stochastic processes or random fields based on covariance functions. In geoscience applications, it is also called a spatial optimal unbiased estimator.

Kriging model is expressed in the stochastic process approach:

$$y(\mathbf{x}^{(i)}) = \mu + \varepsilon(\mathbf{x}^{(i)}), \quad i = 1, \cdots, n \tag{13}$$

where, μ is the mean of the stochastic process, $\varepsilon(\mathbf{x}^{(i)})$ is Normal $(0,\sigma^2)$, which is given by Eqs. (14)–(16).

$$Cov[\varepsilon(\mathbf{x}^{(i)}), \varepsilon(\mathbf{x}^{(j)})] = \sigma^2\mathbf{R}([Corr[\varepsilon(\mathbf{x}^{(i)}), \varepsilon(\mathbf{x}^{(j)})]]) \tag{14}$$

$$Corr[\varepsilon(\mathbf{x}^{(i)}), \varepsilon(\mathbf{x}^{(j)})] = exp[-d(\mathbf{x}^{(i)}, \mathbf{x}^{(j)})] \tag{15}$$

$$d(\mathbf{x}^{(i)}, \mathbf{x}^{(j)}) = \sum_{h=1}^{k} \theta_h |x_h^{(i)} - x_h^{(j)}|^{p_h}, \quad \theta_h \geq 0, \quad p_h \in [1, 2] \tag{16}$$

where, R denote the $n \times n$ matrix whose (i, j) entry is $Corr[\varepsilon(\mathbf{x}^{(i)}), \varepsilon(\mathbf{x}^{(j)})]$,The estimates of the parameters$\mu$and σ^2 have little direct interpretation, as they must be combined with the estimates of the correlation parameters (the θ_h's and p_h's) in order to make predictions.

So, there have $2k+2$ parameters: μ, σ^2, θ_1, $\cdots$, θ_k and p_1, $\cdots$, p_k. We can predict these parameters by choosing them to maximise the likelihood of the samples. Let $\mathbf{y} = (y^{(1)}, \cdots, y^{(n)})'$ denote the n-vector of observed values or numerical calculation results. and 1 denote an n-vector of ones. Then the likelihood function is:

$$\frac{1}{(2\pi)^{n/2}(\sigma^2)^{n/2}|\mathbf{R}|^{\frac{1}{2}}} \exp\left[-\frac{(\mathbf{y}-\mathbf{1}\mu)'\mathbf{R}^{-1}(\mathbf{y}-\mathbf{1}\mu)}{2\sigma^2}\right] \tag{17}$$

Given the correlation parameters θ_h and p_h for $h = 1, \cdots, k$, we can solve for the values of μ and σ^2 that maximise the likelihood function above in closed form:

$$\hat{\mu} = \frac{\mathbf{1}'\mathbf{R}^{-1}\mathbf{y}}{\mathbf{1}'\mathbf{R}^{-1}\mathbf{1}} \tag{18}$$

$$\hat{\sigma}^2 = \frac{(\mathbf{y}-\mathbf{1}\hat{\mu})'\mathbf{R}^{-1}(\mathbf{y}-\mathbf{1}\hat{\mu})}{n} \tag{19}$$

Table 3
Grid convergence results for S60_C3 catamaran model.

F_r	R_t_EFD/N	r_G	R_G	$\varepsilon_{21}\%S_2$	$U_I\%S_2$	$U_G\%S_2$	$U_{SN}\%S_2$	GCI_{12}	GCI_{23}
0.30	12.061	1.414	0.614	0.734	0.078	2.030	2.032	1.468%	2.375%
0.35	17.217	1.414	0.735	0.553	0.080	3.503	3.504	1.931%	2.611%
0.40	43.32	1.414	0.673	0.611	0.048	2.556	2.556	1.584%	2.338%
0.45	67.002	1.414	0.735	0.245	0.043	1.547	1.548	0.851%	1.155%
0.50	81.635	1.414	0.640	0.880	0.054	2.943	2.943	1.978%	3.061%
0.55	93.234	1.414	0.694	0.956	0.045	4.581	4.581	2.732%	3.900%

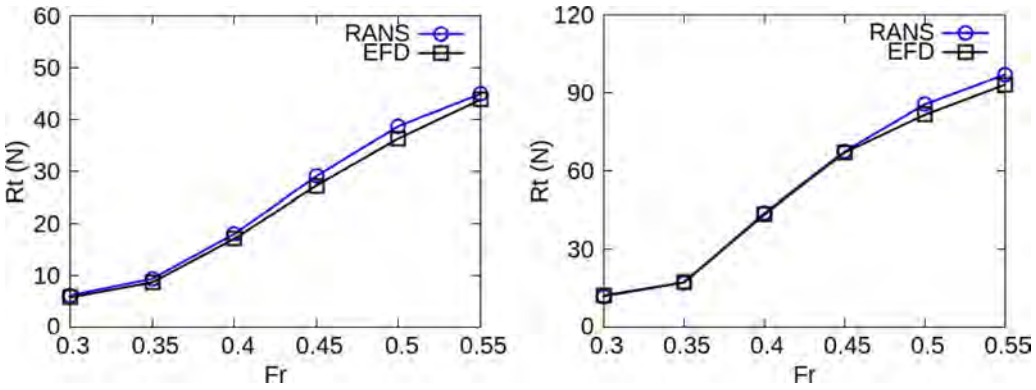

Fig. 11. The resistance values and errors of the S60 monohull (left) and S60_C3 catamaran (right) model.

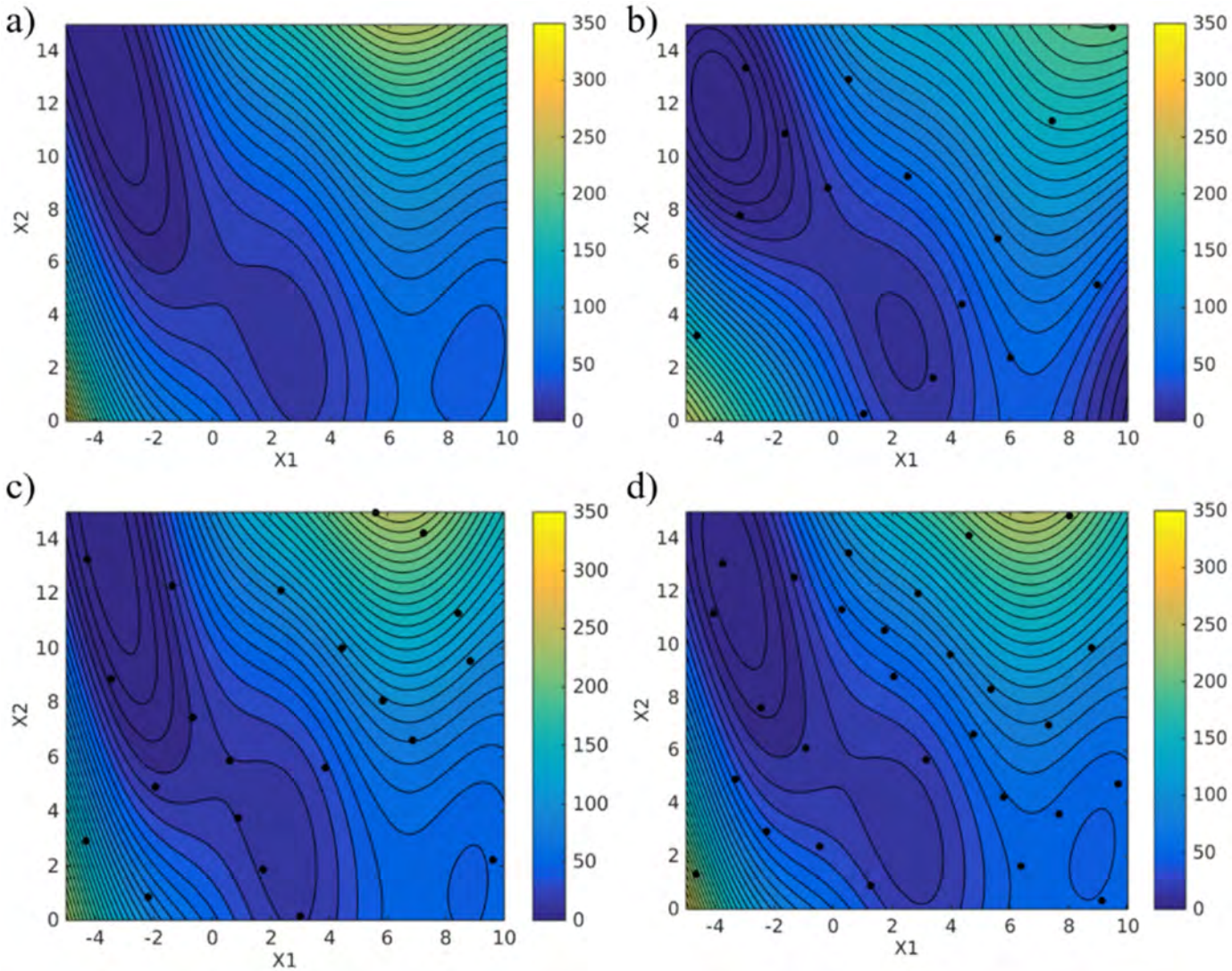

Fig. 12. Comparison of the real function (a) and the corresponding approximation models using 15 samples (b), 21 samples (c) and 28 samples (d).

For any new position x^*, let r denote the n-vector of correlations between the error term at x^* and the error terms at the sample points. That is, $r_i(\mathbf{x}^*) = Corr[\varepsilon(\mathbf{x}^*), \varepsilon(\mathbf{x}^{(i)})]$, computed using the Eqs. (15) and (16). Then, we can calculate the prediction value at the position x^*:

$$\hat{y}(\mathbf{x}^*) = \hat{\mu} + \mathbf{r}'\mathbf{R}^{-1}(\mathbf{y} - \mathbf{1}\hat{\mu}) \tag{20}$$

The number of samples is closely related to the accuracy of Kriging model, which is of vital importance to the optimization results. Approximately $n = 10k$ or $11k - 1$ points in k dimensions were typically sampled in the Kriging model design process, based on the number of sampling points used in previous studies [14]. In this section, a Branin-Hoo modified function is taken as an example. This function is usually used as a case to validate the prediction accuracy of a surrogate

Table 4
Error analysis of approximation models in Fig. 12(b) and (d).

	15 samples	21 samples	28 samples
Max ABS (error)	24.83%	9.47%	5.54%
Avg ABS (error)	1.65%	1.09%	0.86%
root MSE	4.63%	3.14%	2.02%

model and also one of the most common optimization test functions. It is a two-dimensional function and given as follows:

$$f(\mathbf{x}) = a(x_2 - bx_1^2 + cx_1 - r)^2 + s(1-t)\cos(x_1) + s + 5x_1, \quad -5 \le x_1 \le 10,\ 0 \le x_2 \le 15 \tag{21}$$

where $a = 1$, $b = 5.1/(4\pi^2)$, $c = 5/\pi$, $r = 6$, $s = 10$and$t = 1/(8\pi)$.

Fig. 12 shows the contours of the real mathematic function (given by Eq. (21)) and approximation models. Three different numbers of sample points, shown as black dots, are used to construct an approximation model for this function. As can be seen, as the number of sample points increases, the approximate model fits better. And the approximation model based on only 21 sample points is accurate enough to locate the optimum.

To further check the accuracy of the Kriging models, sixty evenly spaced points (not including the sampling points) are taken from within the design space. The maximum absolute error (difference between the actual and predicted values), the average absolute error, and the root mean square error (MSE) [26], which is:

$$\text{root MSE} = \sqrt{\frac{\sum_{i=1}^{n}(y_i - \hat{y}_i)^2}{n}} \tag{22}$$

where n is the number of additional untried sample points. y_i is the actual value, and $\hat{y}_i$ is the predicted value.

The error results of approximation models based on three different numbers of samples for this function are listed on Table 4. Based on the error analysis, it can be concluded that the Kriging model approximated the original functions very well since there are quite low root MSE and 21 samples are enough for a Kriging model construction. The maximum absolute errors are much larger, which may be caused by the fact that some testing points are far from the samples according to the typical behaviour for a Kriging model. So, for an optimization problem, after finding optimal results through the surrogate model, it is also very importance to further validate the optimization results through numerical simulations or experiments.

5. Multi-objective design optimisation of a S60_C3 catamaran

The goal of this study is to optimise the total resistance of a S60_C3 at two speeds by modifying the fore part shape of the demihull and the separation between the demihulls. The multi-objective optimisation procedure is shown in Fig. 13. It begins with the initial catamaran represented by NURBS surfaces. The first step is to determine the number and ranges of ship modification parameters in the FFD method. Based on the DOE method, a set of sample points are created in the design space, where each sample point represents a feasible catamaran design. The computational domain meshes for all sample catamarans are then automatically generated by the mesh tool SnappyHexMesh.

Next, the resistance values for all sample catamarans at two speeds are calculated by the RANS-based solver naoe-FOAM-SJTU. Two approximation models are then built, based on the sample catamarans, and these are used to compute the resistances rather than using computational time-intensive direct numerical prediction. The multi-objective algorithm NSGA-II [36] is used to search the approximation models for optimal solutions, and the optimal catamaran designs are obtained by iterations of this algorithm. Finally, the optimal results are validated by the naoe-FOAM-SJTU solver.

5.1. Selection of design variables, objective functions and constraints

Fig. 14 shows the modification region of a demihull and the control nodes distribution used by the FFD method. In each of Fig. 16a–c, the red points are considered as one group and moved all at once along the x, y and z-axis directions to change the length, width and depth of the

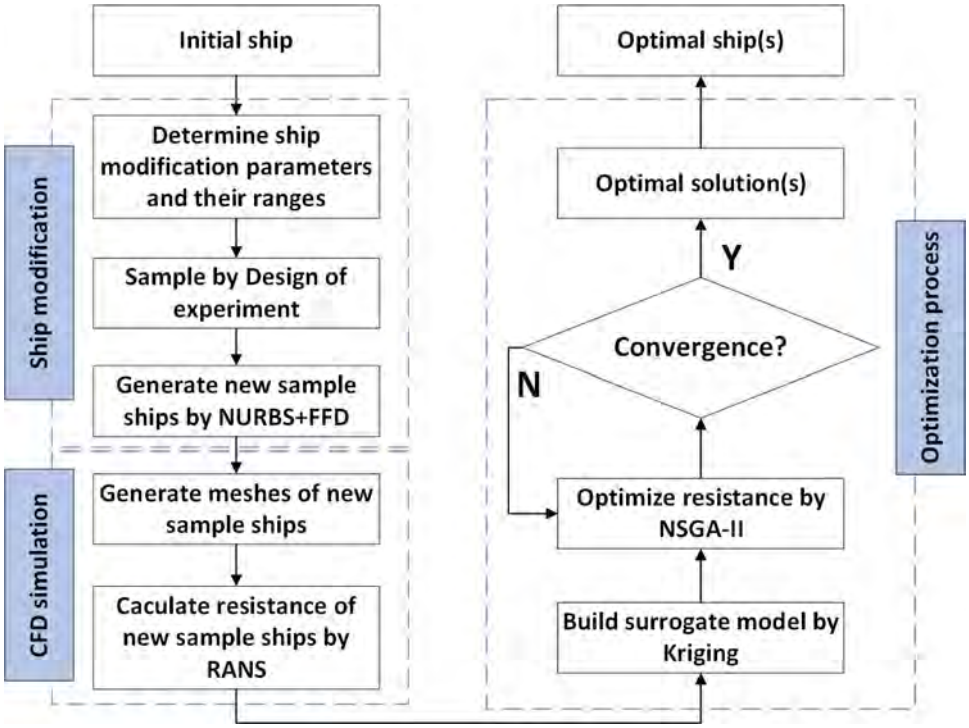

Fig. 13. Flowchart of multi-objective design optimisation for an S60_C3 catamaran, including three main parts: the ship modification, the hydrodynamic performance calculation and the iterative optimisation process.

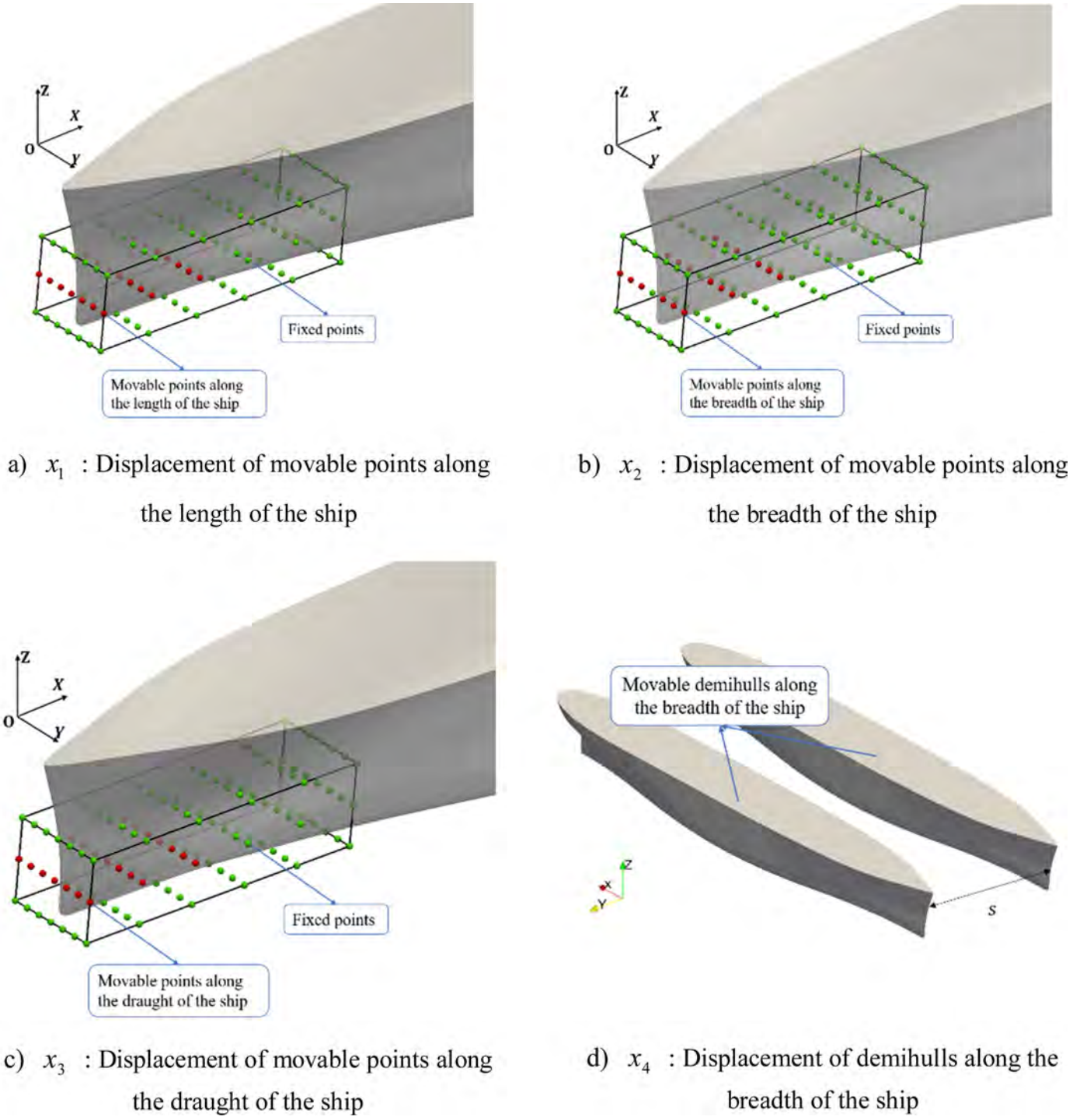

a) x_1 : Displacement of movable points along the length of the ship

b) x_2 : Displacement of movable points along the breadth of the ship

c) x_3 : Displacement of movable points along the draught of the ship

d) x_4 : Displacement of demihulls along the breadth of the ship

Fig. 14. The control points distribution in the lattice based on FFD method.

demihull's bow, respectively, and the green points are fixed. Thus, there are four design variables in total: the displacements of FFD-movable control nodes in three directions and the separation between demihulls. Fig. 15 shows a schematic diagram of deformation of a demihull based on the FFD method. Given a set of values $(x_1, x_2, x_3) = (-0.06, -0.05, -0.03)$, we want to get the deformed hull. The specific deformation process is as follows: first move the red points of Fig. 14a) along the length of the ship by a distance of 0.06, obtaining the deformed hull as shown in Fig. 15b). Then move the red points of Fig. 14b) along the breadth of the ship by a distance of 0.05, obtaining the deformed hull as shown in Fig. 15c). Finally, move the red points of Fig. 14c) along the draught of the ship by a distance of 0.03, and the deformed demihull as shown in Fig. 15d) is obtained. Their upper and lower bounds are presented in Table 5 and scaled by L_{PP} according to Eq. (23).

$$x'_j = x_j / L_{pp}, \quad j = 1, 2, 3, 4 \tag{23}$$

Fig. 16 shows the initial catamaran and five sample catamarans generated by the FFD method. These are obviously different from each other in terms of demihull shape and separation.

The objective functions and geometric constraints for these models

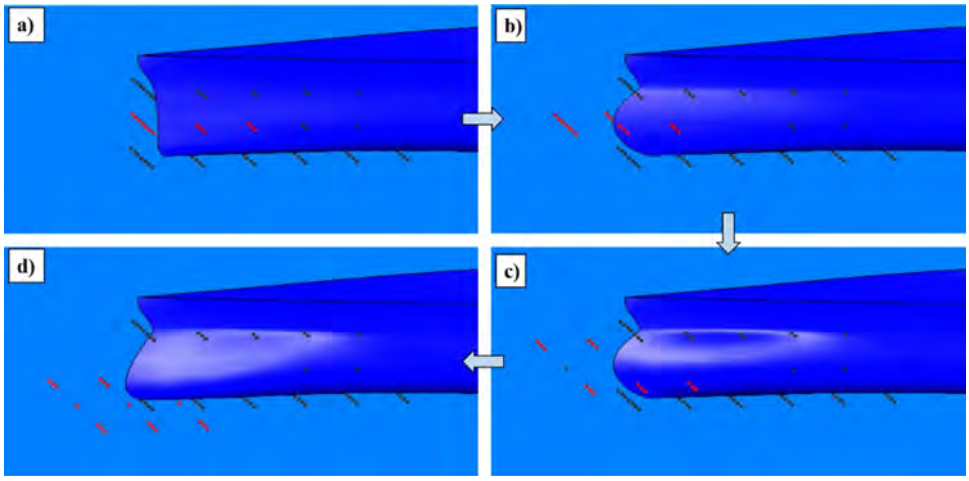

Fig. 15. A diagram of deformation based on FFD method.

Table 5
Design variables and their ranges.

Design variables	Lower bound	Upper bound
x_1	−0.12	0
x_2	−0.05	0
x_3	−0.03	0.01
x_4	0.1	0.25

Note:Non-dimensional design variables.

are expressed in Eq. (24).

$$\min \begin{cases} f_{obj}^1 = R_t, \text{ Fr} = 0.4 \\ f_{obj}^2 = R_t, \text{ Fr} = 0.45 \end{cases} \text{ Subjectto: } \Delta \geq 99\%\Delta_0 \tag{24}$$

5.2. Sensitivity analysis

A preliminary sensitivity analysis is performed, for the resistances at $F_r = = 0.4$ and 0.45. The reductions of the objective functions are shown in Fig. 17. The results show a potential reduction close to 16% and 15% for f_{obj}^1 and f_{obj}^2, respectively. Also, as we can see, the separation between demihulls has a great influence on the resistances. In the case of $F_r = = 0.4$, the effect of the separation between demihulls on resistance is not monotonic. It can be seen that either increasing or decreasing separation is beneficial to the resistance performance. In the case of $F_r = = 0.45$, the effect of spacing on resistance is monotonic. The greater the separation is, the greater the decrease of resistance is. Compared with the separation, the other three design variables have a relatively small impact on resistance. The longer bulb bow is better for the resistance. Of course, the interaction of these variables also has a great and complex influence on the resistance, which is hard to say from Fig. 17.

5.3. Accuracy of approximation models

The approximation models that were built are based on 61 samples. Then, an additional 10 validation ships selected by OLHS method are used to verify the accuracy of the Kriging models. An error is defined as the difference between the actual resistance from numerical simulations and the predicted value from Kriging models. The maximum absolute error, the average absolute error, and the root MSE-from Eq. (22) where n ($= = 10$) is the number of validation ships-from the 10 selected validation ships are summarised in Table 6. Based on the error analysis, it can be concluded that the Kriging models globally approximates the relationship between design variables (ship modification parameters) and objective functions (resistance values) very well since there are quite low root MSE.

5.4. Parameters setup of NSGA-II optimisation algorithm

NSGA-II is a fast and elitist multi-objective genetic algorithm developed based on NSGA [29,5]. The advantages of NSGA-II are its use of

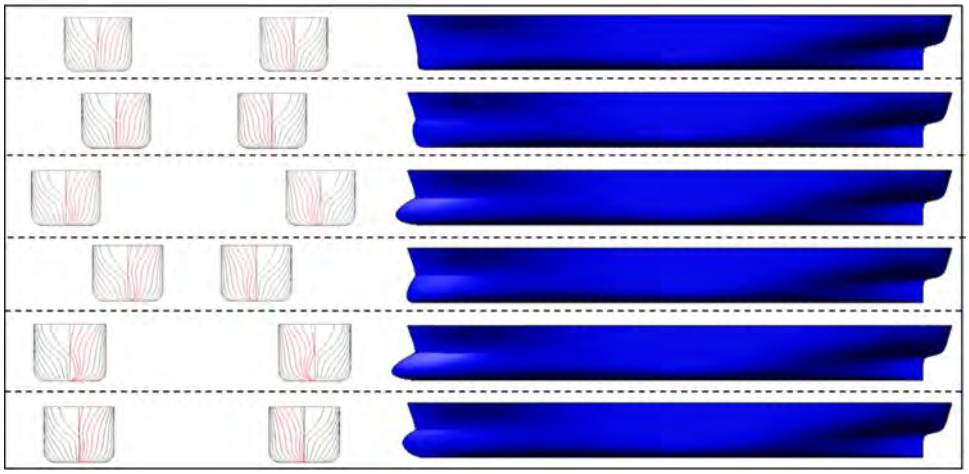

Fig. 16. A diagram of the initial catamaran and sample catamaran designs.

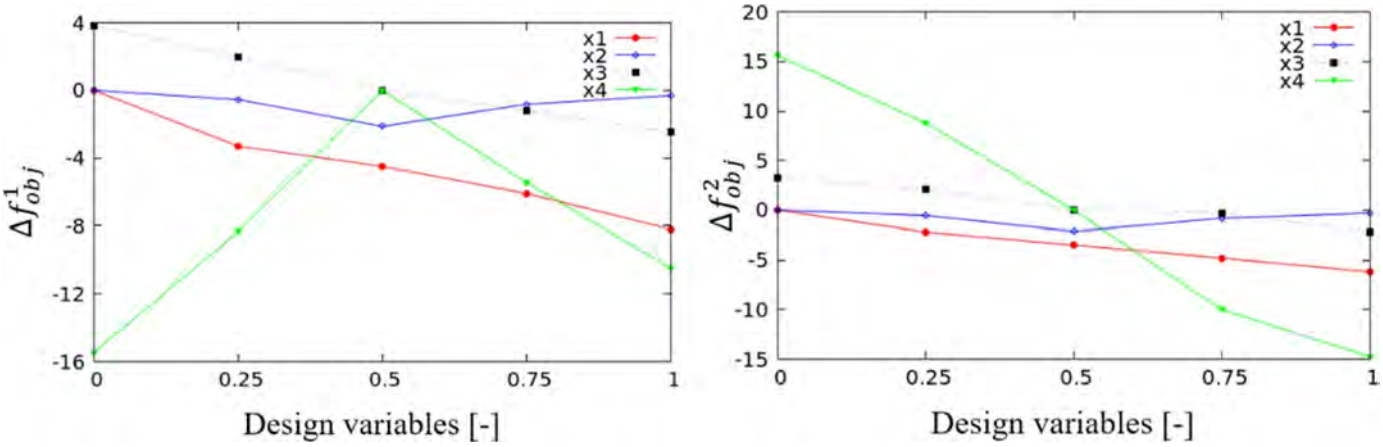

Fig. 17. Sensitivity analysis of the design variables.

Table 6
Error analysis of approximation models.

	R_t (F_r = =0.4)	R_t (F_r = =0.45)
Max ABS (error)	4.05%	3.14%
Avg ABS (error)	1.61%	1.15%
root MSE	2.21%	2.03%

Table 7
The parameters setup of NSGA-II.

Parameters	Values
Size of population	50
Number of generations	400
Crossover fraction	0.8
Migration fraction	0.3
Pareto fraction	0.3

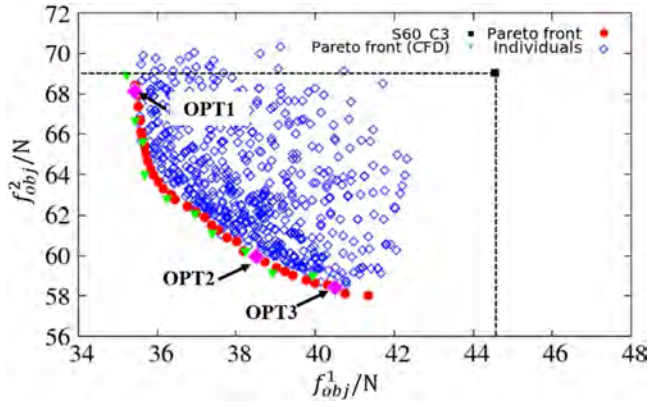

Fig. 18. The Pareto front and the three catamaran candidates selected for further numerical simulations.

non-dominated sorting and crowing distance that enable all optimal solutions to be kept. According to Deb et al. [5], for a constrained multi-objective optimization problem, the definition of dominance has been extended. The validation of NSGA-II in the OPTShip-SJTU solver is given in the literature [36]. Herein, the NSGA-II is used to search for the minimum resistance at two speeds on the approximation models constructed in advance. The parameters setup of NSGA-II is displayed in Table 7.

5.5. Comparative analysis of resistance and flow between the optimal and initial designs

NSGA-II is run ten times, which leading to ten sets of optimal solutions. A non-dominated sorting is applied to all these solutions. And we obtain the Pareto set, which are those solutions that cannot be improved in any of their objectives without degrading at least one of their other objectives (as shown in Fig. 18). Each optimal solution represents an optimal catamaran. Ten optimal solutions selected on the Pareto set (red dots in Fig. 18) are numerically calculated by the RANS solver, naoe-FOAM-SJTU, which are shown in green triangles in Fig. 18. These CFD results are generally consistent with the results of the approximate model.

For further validation of the optimal results, three typically optimal solutions amongst them are selected: OPT1, OPT2 and OPT3. Their demihull shapes and separation configuration are compared to those of the initial catamaran (S60_C3) in Fig. 19. OPT1-3 have a longer bow, the bows of OPT2 and 3 are much fatter than that of S60_C3 and the bow of OPT1 is slightly upturned. OPT2 and OPT3 have a larger separation than S60_C3, and OPT1 has a smaller separation. Details of the hull change of the optimal catamarans are shown in Table 9. The wetted surface area and displacement of the optimal hulls are increased, within the constraints in Eq. (22).

Three above optimal catamarans are directly simulated with the RANS-based naoe-FOAM-SJTU solver. Table 8 shows comparisons of the total resistance of optimal hulls between CFD and Kriging predictions. As can be seen from the errors, the Kriging-based predictions results agree well with the CFD-based numerical results, although the maximum prediction error is 2.695%. Table 9 presents comparisons of the total resistance of the initial and optimal catamarans. For F_r = 0.4, the total resistance of OPT1 has the largest reduction (20.52%), and the other two catamarans also have significant reductions (12.60% and 10.84%). For F_r = 0.45, the total resistance of OPT2 and OPT3 are clearly reduced (15.00% and 13.11%, respectively), but the total resistance of OPT1 is slightly increased. Table 10 shows comparisons of the wetted surface area and displacement of the initial and optimal catamarans. All optimal catamarans have a larger wetted surface area and displacement.

Figs. 20 and 21 show a comparison of the wave elevation of the three optimised catamarans and the initial catamaran for F_r = 0.4 and 0.45. First of all, the bow wave amplitudes of the three optimised ships at both speeds are significantly reduced. This is mainly because the optimised hulls have a bulbous bow, and its generated waves are superimposed with the ship waves to play a role of wave elimination. Besides, in the case of F_r = 0.4, the smaller separation of the OPT1 demihulls causes wave interference to occur in advance between the hulls, resulting in a very different wave system to the initial catamaran.

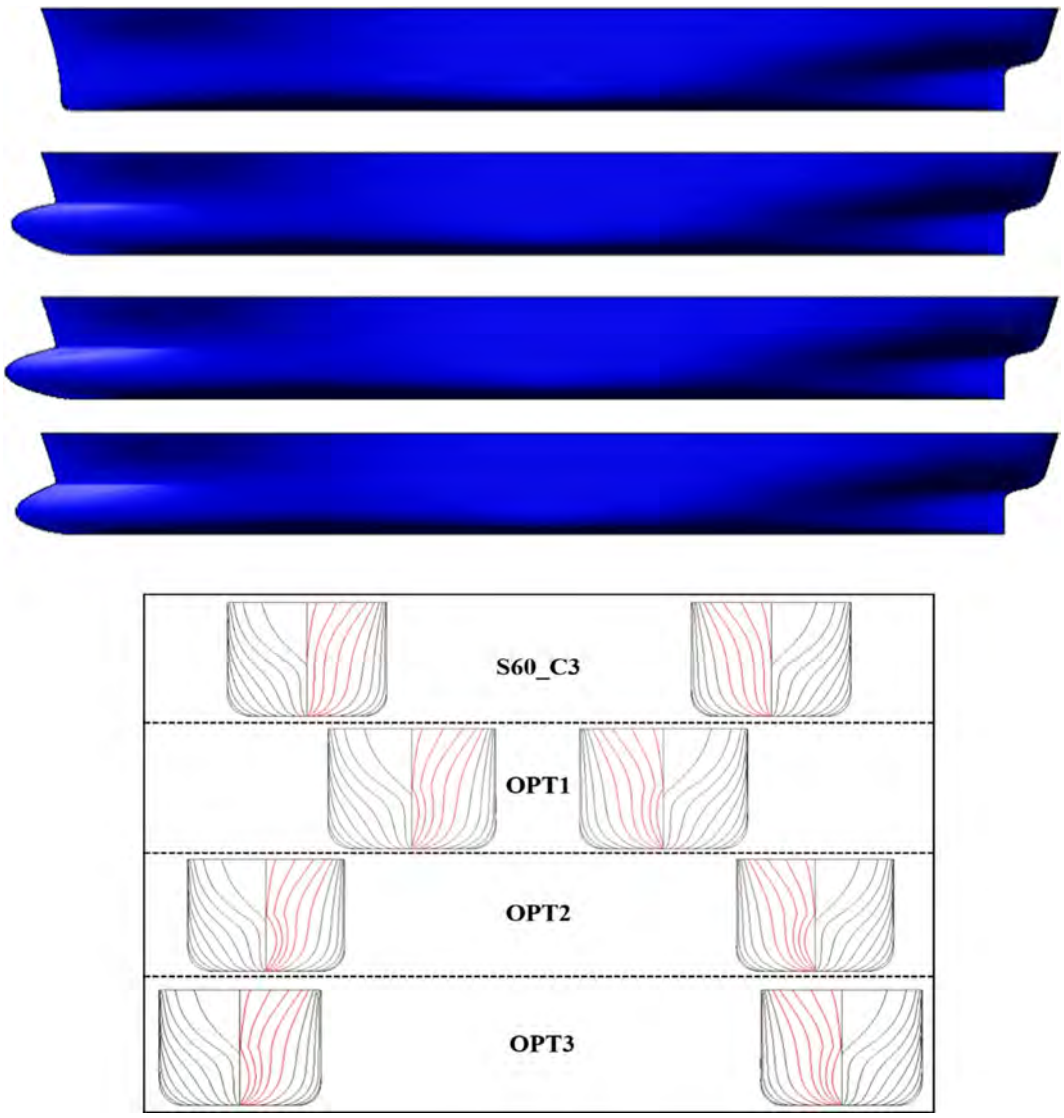

Fig. 19. Comparison of the initial and the optimal (OPT1, OPT2, OPT3) catamarans, including the demihull shapes and separations.

Table 8
Comparison of the resistance results for optimal hulls between CFD and Kriging.

/	R_t (Fr = 0.4)			R_t (Fr = 0.45)		
	CFD	Kriging	Error (%)	CFD	Kriging	Error (%)
OPT1	35.418	35.533	0.323	69.126	68.058	−1.546
OPT2	38.946	38.435	−1.311	58.661	59.807	1.953
OPT3	39.730	40.434	1.771	59.965	58.349	−2.695

Table 10
The geometrical parameters comparison of the demihulls.

	Wetted surface area		Displacement	
	Value [-]	Variation [%]	Value [-]	Variation [%]
S60_C3	1.0620	/	0.0664	/
OPT1	1.0938	3.00	0.0671	1.05
OPT2	1.1006	3.64	0.0676	1.76
OPT3	1.0956	3.16	0.0674	1.57

Table 9
Summary of the optimal results, including design variables and objective functions.

/	Design variables (non-dimensional)				R_t (Fr = 0.4)		R_t (Fr = 0.45)	
	x	y	z	s	Value [N]	Δf^1_{obj}(%)	Value [N]	Δf^2_{obj}(%)
S60_C3			/		44.559	/	69.011	/
OPT1	−0.102	0.000	0.010	0.100	35.418	−20.52	69.126	0.17
OPT2	−0.116	−0.024	0.002	0.233	38.946	−12.60	58.661	−15.00
OPT3	−0.093	−0.024	−0.007	0.249	39.730	−10.84	59.965	−13.11

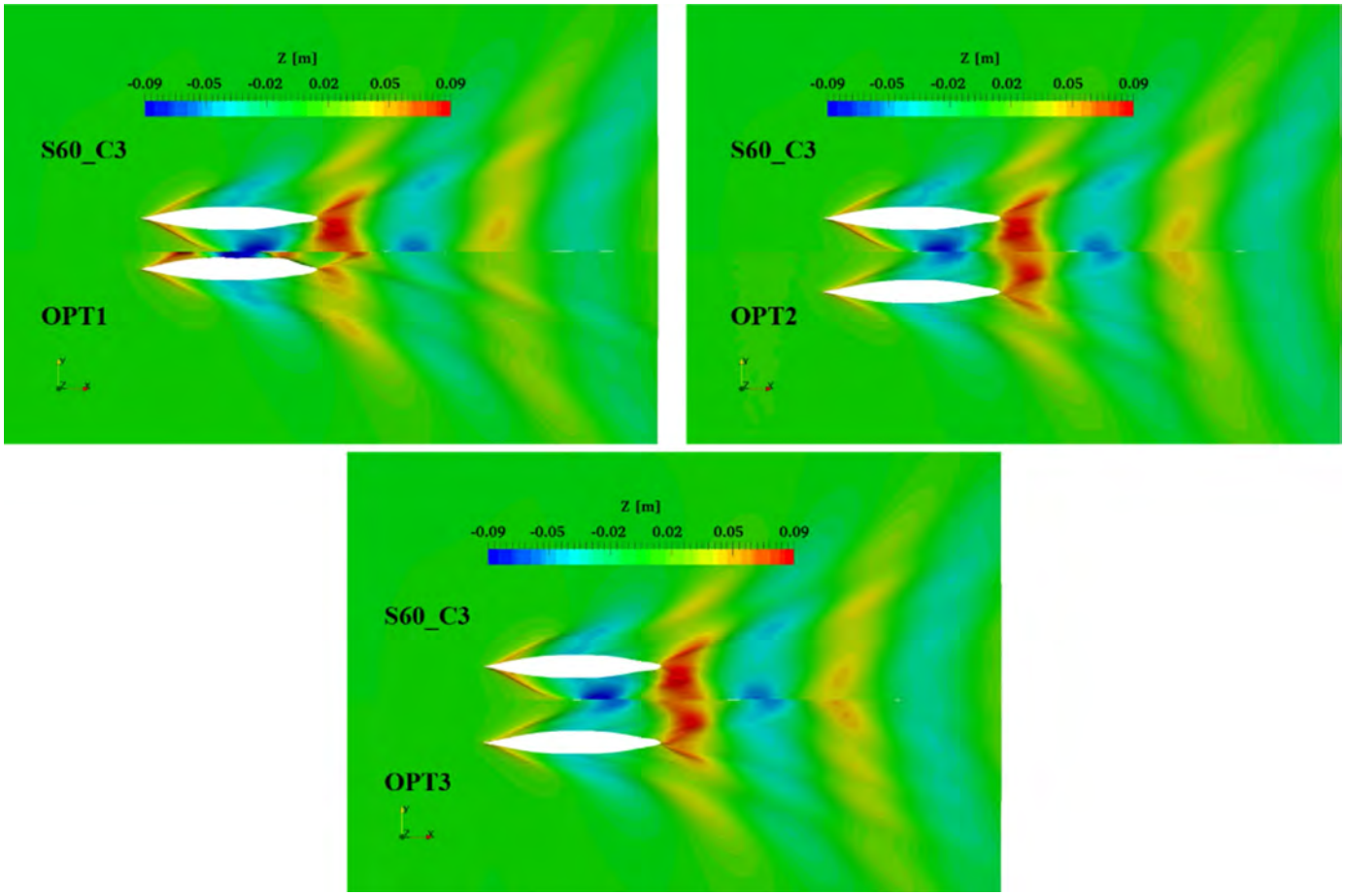

Fig. 20. The wave patterns of the optimal catamarans (upper left: OPT1; upper right: OPT2; lower centre: OPT3) compared to the initial catamaran (S60_C3) at $F_r = 0.4$.

The wave trough of the bow wave system of OPT1 eliminates the wave crest at the stern, and both transverse and diverging wave elevation behind the stern are greatly reduced compared to the initial catamaran. This indicates that OPT1 has a favourable wave interference. The wave interference of OPT2 and OPT3 are similar: the bow wave crest and the first wave trough are reduced compared with those of the initial catamaran. With $F_r = 0.45$, the wave interference between OPT1 demihulls is very similar to that with $F_r = 0.4$, with the only difference being that the stern wave crest appears in advance. The wave elevations of OPT2 and OPT3 are similar to those with $F_r = 0.4$.

Figs. 22 and 23 show a comparison of the pressure distribution between the initial and the optimised catamarans' right demihull. The interference phenomenon means that the pressure distribution on the left and right sides of the demihull is asymmetric, which also affects the resistance.

For $F_r = 0.4$, the longitudinal pressure gradients on the portside of the right demihulls of the optimised catamarans are different from those on the initial catamaran. OPT1 has a smaller low-pressure area due to having a larger wave trough, and there is a pressure recovery at the stern, which means it has a lower longitudinal pressure gradient. The amplitudes of the high- and low-pressure regions of OPT2 and 3 are reduced, leading to a decrease in the longitudinal pressure gradients for these designs. On the starboard side of the right demihull of the optimised catamarans, the longitudinal pressure gradient is little changed. The low-pressure value of OPT1 is increased, and the high-and low-pressure amplitudes of OPT2 and OPT3 are slightly reduced.

For $F_r = 0.45$, the longitudinal pressure gradients on the starboard side of the right demihulls of the optimised catamarans are different from those of the initial catamaran. The high- and low-pressure amplitudes of OPT1, 2 and 3 are reduced, and all the longitudinal pressure gradients are decreased. The longitudinal pressure gradients on the starboard side of the right demihulls remain little changed. The high- and low-pressure amplitudes of OPT1 are slightly increased, and the high-pressure amplitudes of OPT2 and 3 are slightly decreased.

Fig. 24 shows a comparison of cross flow between the initial and the optimised catamarans' right demihull. There is a transverse pressure gradient (See Figs. 22 and 23) due to the asymmetry of the pressure distribution on the two sides of the demihull, so that cross flow is generated, from the portside to the starboard side of the right demihull and vice versa, around the keel of the demihulls. According to the literature [8], cross flow also has an effect on the total resistance.

For OPT2 and OPT3, although the overall shapes of cross flow are generally consistent, cross flow of these two optimised catamarans are weaker than those of the initial catamaran, which reduces the wave interference between the demihulls. Thus, the total resistances are reduced. The main reason should be that the larger separations between the optimised demihulls.

For OPT1, cross flow at two speeds are significantly stronger than those of the initial catamaran, which has a negative effect on the total resistance. However, at two speeds, the shapes of cross flow change differently. For $F_r = 0.4$, cross flow occurs around midship section and the stern shoulder. Around midship section, water flows from the starboard side of the right demihull (outside the demihull) to the portside of the right demihull (inside the demihull), which increases the wave height between the demihulls. Then around the stern shoulder, water flows from the portside of the right demihull to the starboard side, which decreases the wave height between the demihulls. As can be seen from Fig. 24, the wave crest around stern decreases significantly,

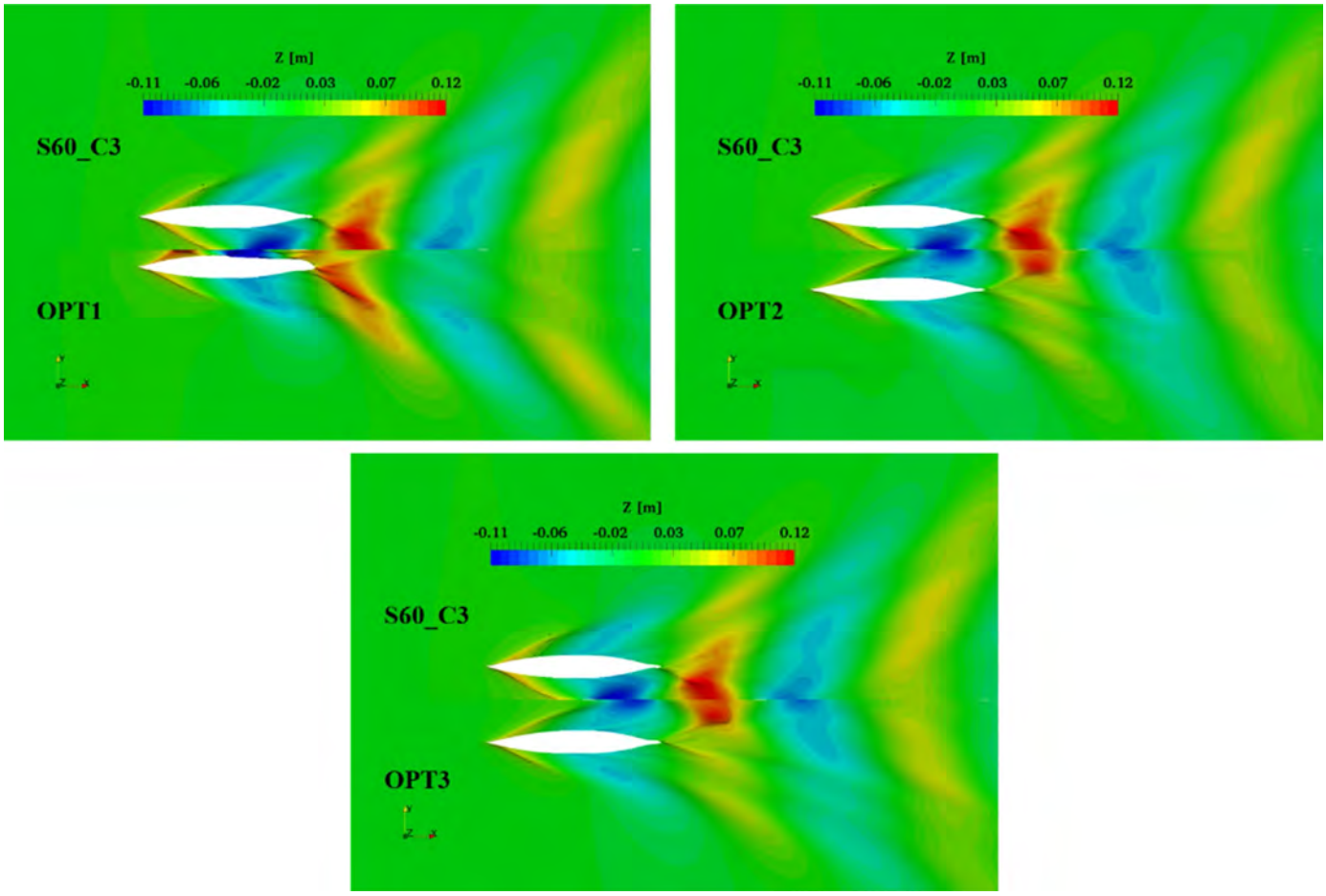

Fig. 21. The wave elevations of the optimal catamarans (upper left: OPT1; upper right: OPT2; lower centre: OPT3) compared to the initial catamaran (S60_C3) at $F_r = 0.45$.

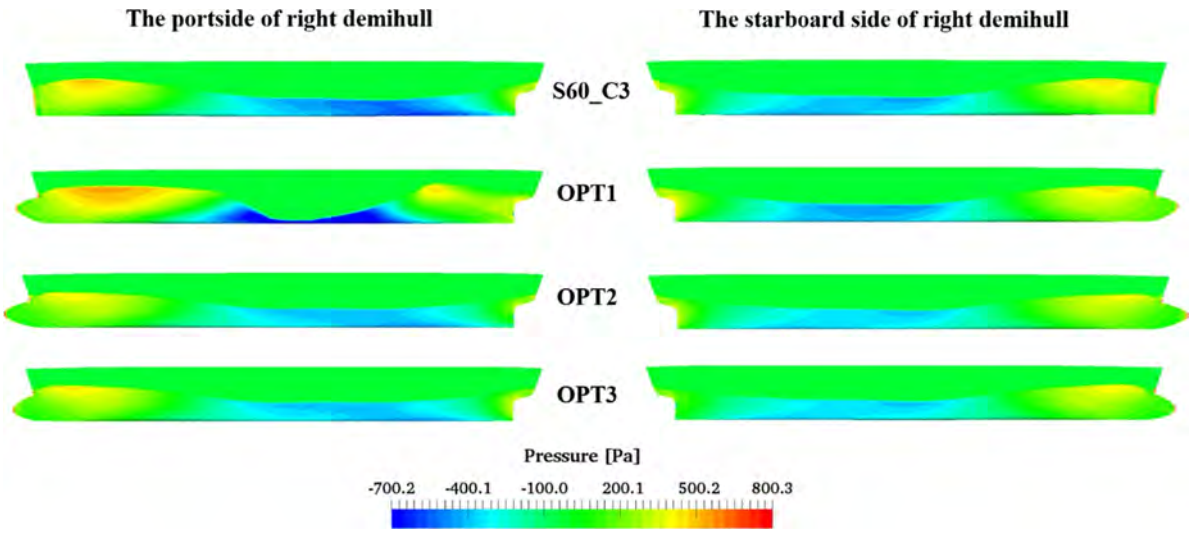

Fig. 22. The pressure field distributions of the optimal catamarans compared to those of the initial catamaran at $F_r = 0.4$.

resulting in a lower total resistance value. For $F_r = 0.45$, cross flow only happens around midship section, where water flows from the starboard side of the right demihull to the portside of the right demihull, leading to a small wave crest around the stern shoulder. This wave spread towards the stern and doesn't weaken the wave crest generated by the stern. So, it doesn't contribute to the reduction of the total resistance.

To further investigate the respective contributions of a demihull shape and separation to the total resistance reduction, three monohull designs are numerically simulated: OPT1_mono, OPT2_mono and OPT3_mono. Table 11 summarises the total resistance of this series of monohulls. Compared to S60_mono, OPT1_mono, OPT2_mono and OPT3_mono all have a reduced total resistance for $F_r = 0.4$ and 0.45. Thus, the shape of three new demihulls have reduced total resistance.

Figs. 25 and 26 show a comparison of the wave elevation of the

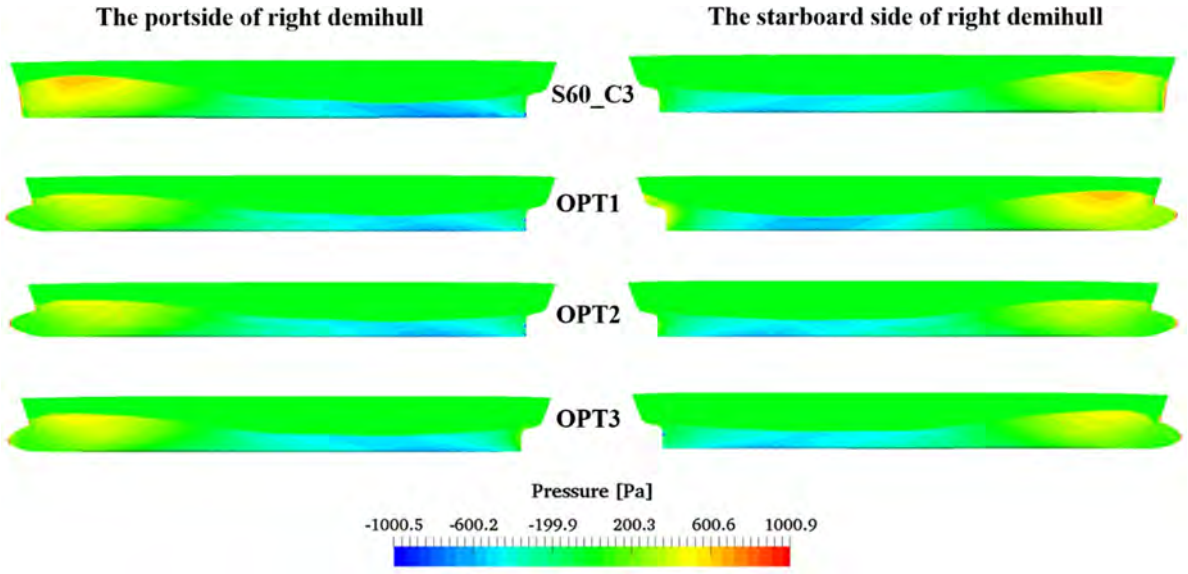

Fig. 23. Pressure field distribution of the optimal catamarans compared to the initial catamaran at F_r = 0.45.

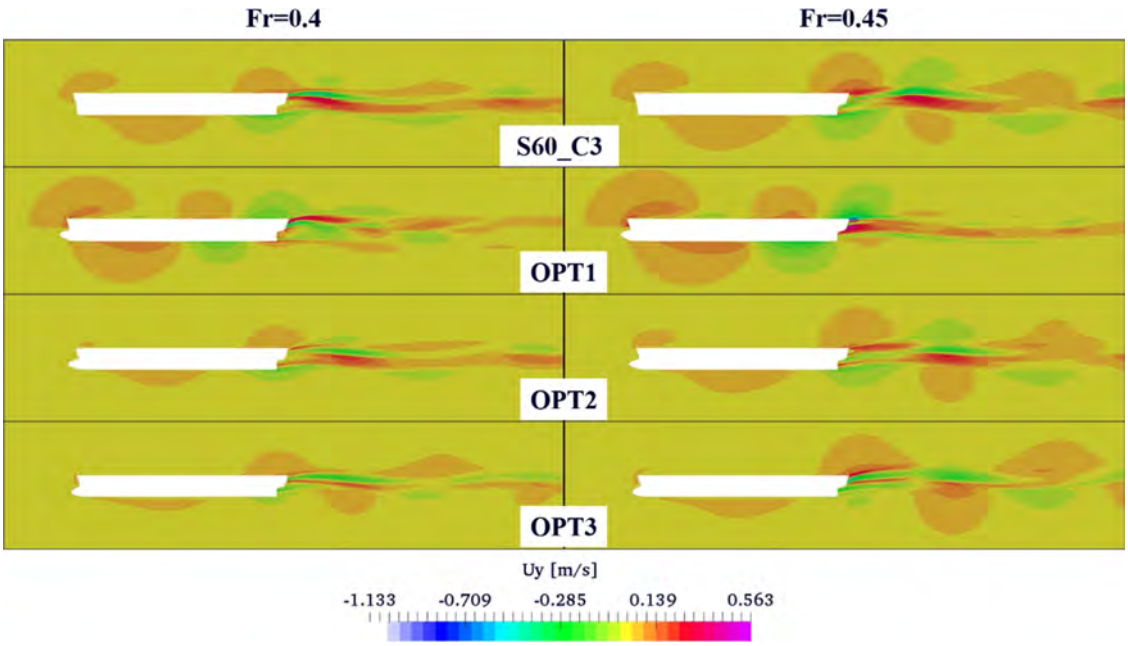

Fig. 24. The cross flow of the optimal catamarans (OPT1, OPT2 and OPT3) compared to the initial catamaran (S60_C3) at two speeds.

Table 11
Comparisons of the four monohulls' resistances.

	R_t (F_r=0.4) Value [N]	Variation (%)	R_t (F_r=0.45) Value [N]	Variation (%)
S60_mono	18.191	/	27.901	/
OPT1_mono	17.069	−6.17	26.968	−3.34
OPT2_mono	16.615	−8.66	26.482	−5.09
OPT3_mono	16.694	−8.23	26.651	−4.48

optimal monohulls, OPT1–1_mono, OPT1–2_mono and OPT1–3_mono (OPT1–3_monos), and S60_mono. OPT1–3_monos all have a lower bow wave compared to the initial S60_mono both for F_r = 0.4 and 0.45, which cause their total resistance to be lower. Figs. 27 and 28 show a comparison of the pressure distributions of OPT1–3_monos and S60_mono. At F_r = 0.4, 0.45, the high-pressure amplitude and areas on the bows of OPT1–3_monos are significantly lower than those on S60_mono. The low-pressure amplitude of OPT1–3_monos are also slightly lower. In addition, the longitudinal gradient of pressure distribution is reduced in OPT1–3_monos, which also contributes to a reduction in the total resistance.

Therefore, in combination with Tables 9 and 11, in the cases of F_r = 0.4 and 0.45, the demihulls' shapes should have a longer, wider and straight or slightly upturned bulb bow, which is advantageous for resistances.

The interference resistance is the difference between the total resistance of catamaran and the double total resistance of a monohull [8]. The interference factor *IF* is defined as the ratio between the interference resistance and the double total resistance of monohull, as given by Eq. (25).

$$IF = \frac{R_{T,C} - 2R_{T,MH}}{2R_{T,MH}} \tag{25}$$

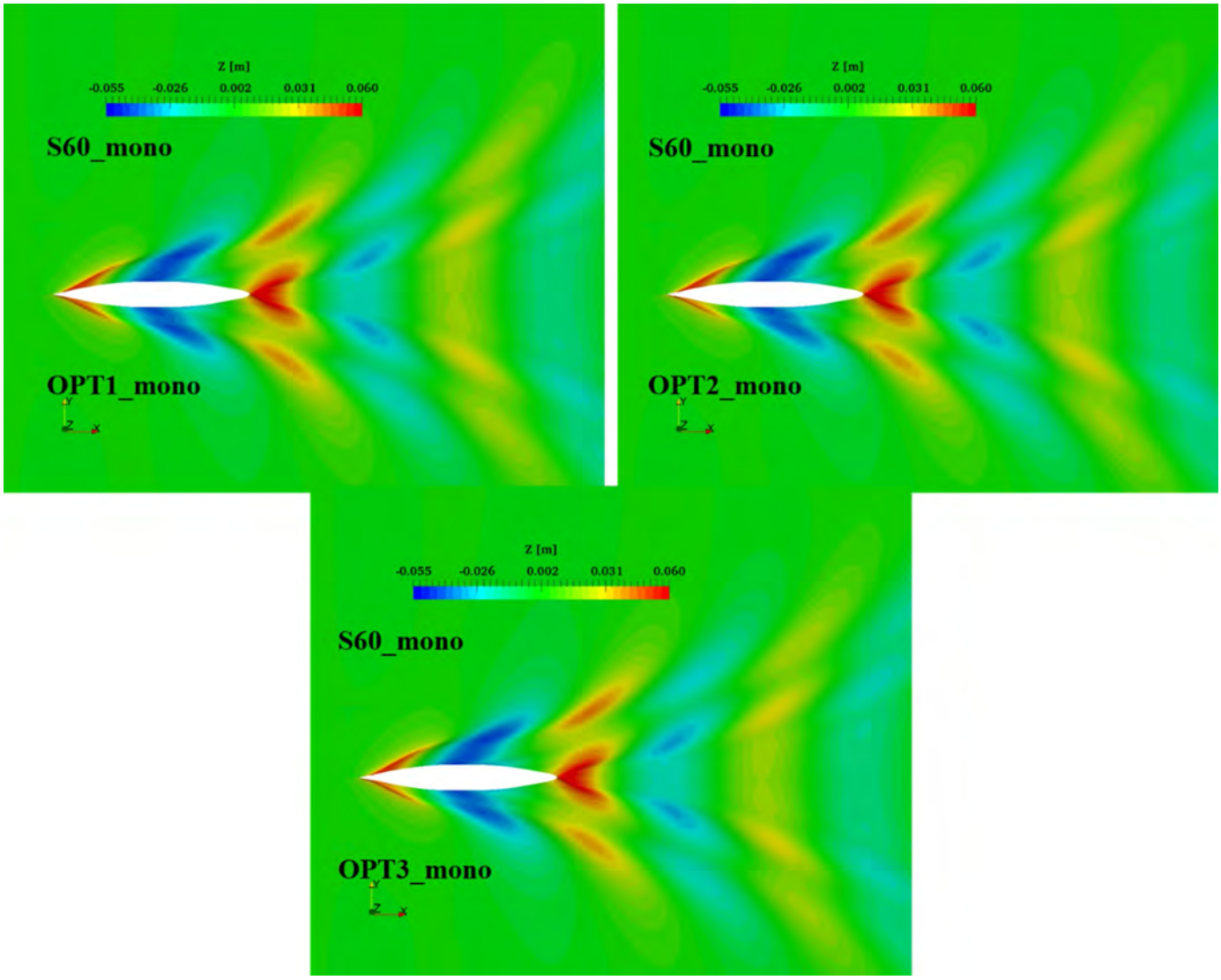

Fig. 25. The wave elevations of the optimal monohulls (upper left: OPT1_mono; upper right: OPT2_mono; lower centre: OPT3_mono) compared to those of the initial S60 monohull (S60_C3) at $F_r = 0.4$.

where $R_{T,C}$ is the total resistance of the catamaran and $R_{T,MH}$ is the total resistance of the monohull.

Table 12 shows the *IF* values of the initial and optimal catamarans. As can be seen, the *IF* values of the initial catamaran are large both when $F_r = 0.4$ and 0.45. Specifically, the total resistance increases by 22.48% and 23.67% for Fr = 0.4 and 0.45, respectively, due to interference phenomena. After optimisation, all optimal catamarans have a smaller *IF* value, except OPT1 for $F_r = 0.45$. Notably, the *IF* value of OPT1 for $F_r = 0.4$ is considerably reduced, to 3.75%. In addition, the wave elevation of OPT1 in Fig. 19 is visibly much more reduced than that of the other catamarans. In contrast, the *IF* value of OPT1 for $F_r = 0.45$ is significantly greater, leading to a slight increase in the total resistance (as shown in Table 9).

Longitudinal wave cuts along the centreline of the initial and optimised catamarans (black solid lines) are compared to those of the corresponding monohulls (blue dashed lines) at the distance $y = s/2$ from the centreline of the monohulls for $F_r = 0.4$, 0.45, shown in Fig. 29. It is important to note that wave cuts for the monohull were doubled. Differences in the wave cuts between the catamaran and the monohull visually reveal the wave interference. OPT1 has a large interference both at $F_r = 0.4$ and 0.45. At $F_r = 0.4$, the bow wave crest of OPT1 is higher and the stern wave is lower than those of the monohull, which is a favourable interference for resistance. At $F_r = 0.45$, the wave amplitudes of both OPT1 and the monohull are much higher, leading to greater resistance. For OPT2 and OPT3 with $F_r = 0.4$ and 0.45, the wave cuts between the catamaran and the monohull are more consistent compared with those of the initial catamaran and the monohull, which illustrates the reduced interference of OPT2 and OPT3 in these conditions. In addition, a lower wave elevation can be seen in the wave cuts comparison between the initial and the optimal catamarans.

In summary, the shape of the optimised demihulls all have a longer, fatter, flatter bulb bow. Such shapes reduce the high pressure area of the mother demihulls (See Figs. 27 and 28). Overall, the effect of shapes on total resistance is consistent in the case of $F_r = 0.4$ and 0.45 (see Table 11). Compared with the demihulls' shape, the separation has a larger influence on resistance, and the influence is inconsistent in the case of $F_r = 0.4$ and 0.45 (See Fig. 17 and Table 12). It is possible to reduce the unfavourable wave interference between the demihulls with larger or smaller separations when $F_r = = 0.4$ (See Figs. 20 and 29), and when $F_r = = 0.45$, larger separations are advantageous for the resistance performance (See Figs. 21 and 29). The pressure amplitudes on the surface of the demihulls are generally reduced (See Figs. 22 and 23). Both at $F_r = = 0.4$ and 0.45, when the separation becomes large enough, the more undisturbed flow between the demihulls happen and

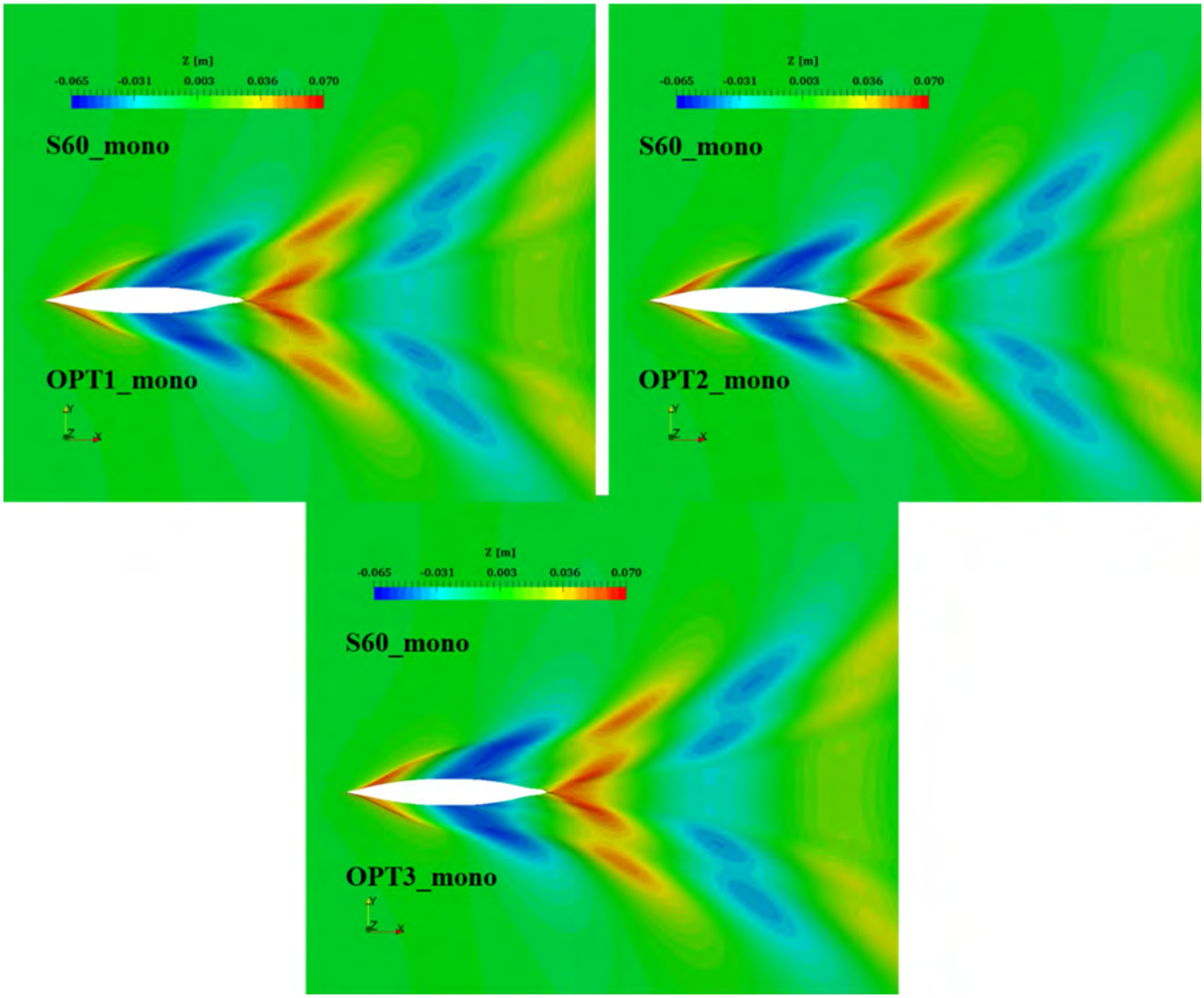

Fig. 26. The wave patterns of the optimal monohulls (upper left: OPT1_mono; upper right: OPT2_mono; lower centre: OPT3_mono) compared to those of the initial S60 monohull (S60_C3) at $F_r = 0.45$.

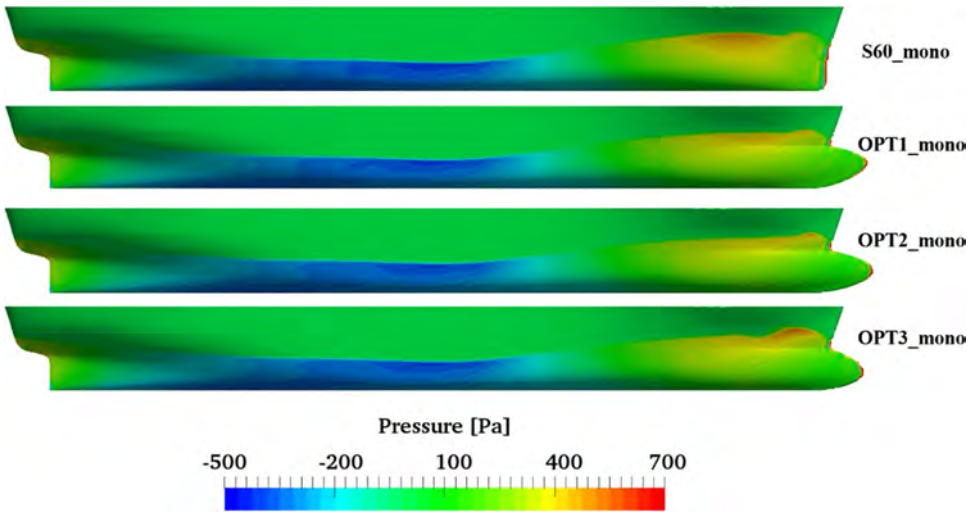

Fig. 27. The pressure field distribution of the optimal monohulls compared to that of the initial monohull at $F_r = 0.4$.

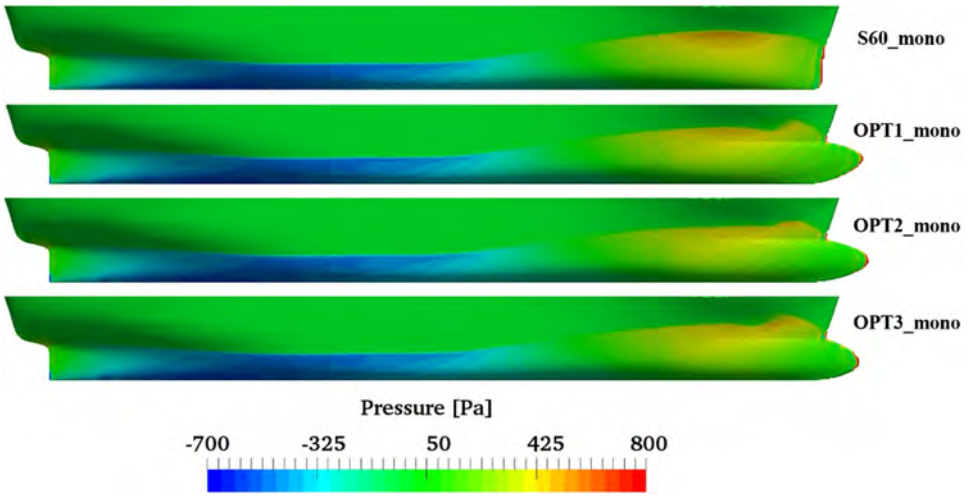

Fig. 28. The pressure field distribution of the optimal monohulls compared to that of the initial monohull at $F_r = 0.45$.

Table 12
Deviation of *IF* values of the initial and optimal catamarans.

	IF (F_r=0.4)		*IF* (F_r=0.45)	
	Value [-]	Variation (%)	Value [-]	Variation (%)
S60_C3	0.2248	/	0.2367	/
OPT1	0.0375	−83.33	0.2816	18.97
OPT2	0.1720	−23.46	0.1076	−54.55
OPT3	0.1900	−15.49	0.1250	−47.20

the cross flow is greatly reduced (See Fig. 24), which also contributes to the resistance performance.

6. Conclusions

This study is a multi-objective design optimisation of the shape and separation of the demihulls of a catamaran. The FFD method is applied to smoothly and flexibly modify the NURBS surfaces of the demihull. On account of the complex interference which occurs between demihulls, a RANS method is used for hydrodynamic simulations. NSGA-II is successfully applied to obtain the optimal catamarans. Kriging-based approximation models are built and used for the prediction of total resistance, rather than performing a more time-intensive and computationally expensive numerical calculation.

The OPTShip-SJTU solver incorporating three main modules – ship modification, hydrodynamic evaluation and optimisation – has been further developed and successfully applied to a multi-objective design optimisation of a catamaran. The initial catamaran is represented by NURBS surfaces, which are then flexibly and locally modified by an FFD method. The optimal catamarans are represented by NURBS surfaces rather than discretised meshes. A RANS-based solver, naoe-FOAM-SJTU, proves well-suited for the hydrodynamic evaluation of the catamarans. The Pareto front is obtained by the NSGA-II on approximation model, and the further comparative analysis of the hydrodynamics of the initial and the optimal catamarans confirm the effectiveness of the ship hull optimisation tools developed in the OPTShip-SJTU solver.

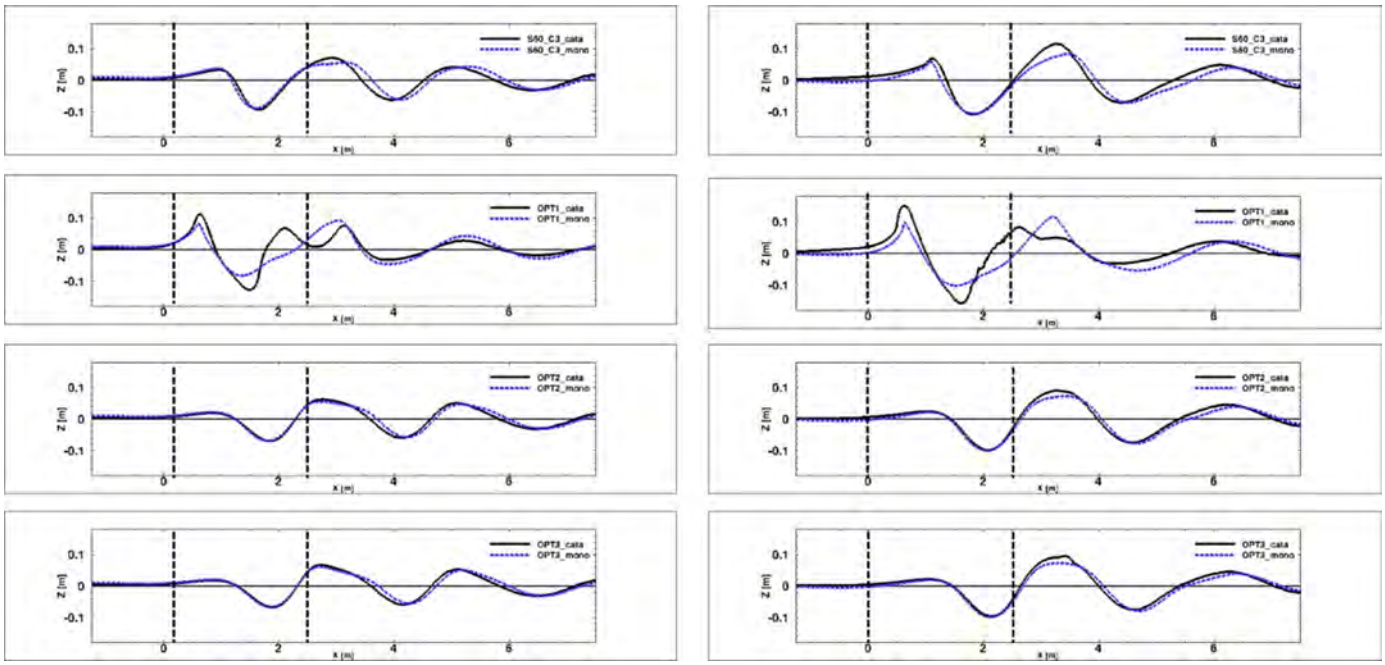

Fig. 29. Longitudinal wave cuts for the initial and the optimised catamarans at $F_r = 0.4$ (left) and $F_r = 0.45$ (right). The two black dashed lines bracket the section of the ship which was compared.

Based on the OPTShip-SJTU solver, a maximum resistance reduction of 20.52% for OPT1 and 15.00% for OPT2 are achieved by the optimal catamaran designs for $F_r = 0.4$ and 0.45, respectively. Three optimal catamaran designs are selected from the Pareto front for numerical simulations using RANS-based solver naoe-FOAM-SJTU. The hydrodynamics of these catamarans are compared in detail to those of the initial catamaran. The total resistances of the three optimal catamarans are greatly reduced at $F_r = 0.4$, and the total resistance of OPT1 is increased a little (0.17%) at $F_r = 0.45$, due to a larger *IF* value (see Table 12). The contributions of different demihull shapes and separation distances to the total resistance reduction are also investigated. All demihull shapes have a favourable, reducing effect on the total resistance, as shown in Table 9. All optimal demihull separations reduce the wave interference except that of OPT1 (see Table 12).

Although the results of this study are positive, there are several drawbacks. First, the deformation region of the demihulls is small. The change of the wave elevation and pressure distribution is obvious but small, but the deformation region can in reality be larger, such as is seen in the whole demihulls, which can change the wave elevation and pressure distribution to a greater extent. Second, the two demihulls of the catamaran are assumed to be symmetric in deformation; in contrast, it will be necessary and very interesting to examine the effects of asymmetric demihull deformation. That is, asymmetric deformation may enable more favourable wave interference to be established between demihulls, affording optimised catamaran designs with better resistance performance.

The above two aspects will lead to another problem: when the number of the deformation parameters increase, the number of sample catamarans that will be generated for the approximate model construction will increase, which will inevitably increase the time and cost of CFD simulations. Therefore, future work will involve continued optimisation of the resistance of the catamaran by using FFD method that independently changes the two sides' shape of the demihulls. In order to avoid the time commitment and expense of a numerical calculation method, a dynamic approximation model [27,7] and a ParEGO method [15,19] will be utilised.

CRediT authorship contribution statement

Aiqin Miao: Conceptualization, Methodology, Software, Writing - original draft, Data curation, Visualization, Investigation, Validation. **Min Zhao:** Data curation, Visualization, Investigation, Validation. **Decheng Wan:** Supervision, Investigation, Validation, Writing - review & editing.

Declaration of Competing Interest

None.

Acknowledgements

This work is supported by the National Natural Science Foundation of China (51879159), The National Key Research and Development Program of China (2019YFB1704204), Chang Jiang Scholars Program (T2014099), Shanghai Excellent Academic Leaders Program (17XD1402300), Innovative Special Project of Numerical Tank of Ministry of Industry and Information Technology of China (2016-23/09) and Lloyd's Register Foundation for doctoral student, to which the authors are most grateful.

References

[1] M.D. Buhmann, Radial basis functions, Acta Numer. 9 (5) (2000) 1–38.
[2] E.F. Campana, D. Peri, Y. Tahara, F. Stern, Shape optimization in ship hydrodynamics using computational fluid dynamics, Comp. Meth. Appl. M. 196 (1–3) (2006) 634–651.
[3] X. Chen, M. Diez, M. Kandasamy, Z. Zhang, E.F. Campana, F. Stern, High-fidelity global optimization of shape design by dimensionality reduction, metamodels and deterministic particle swarm, Eng. Optimiz. 47 (4) (2015) 473–494.
[4] X. Cheng, B. Feng, Z. Liu, H. Chang, Hull surface modification for ship resistance performance optimization based on Delaunay triangulation, Ocean Eng. 153 (2018) 333–344.
[5] K. Deb, S. Agrawal, A. Pratap, T. Meyarivan, A fast elitist non-dominated sorting genetic algorithm for multi-objective optimisation: NSGA-II, Conference on Parallel Problem Solving from Nature (PPSN VI), 2000, pp. 849–858.
[6] M. Diez, A. Serani, E.F. Campana, O. Goren, K. Sarioz, D.B. Danisman, G. Grigoropoulos, E. Aloniati, M. Visonneau, P. Queutey, F. Stern, Multi-objective hydrodynamic optimization of the dtmb 5415 for resistance and seakeeping, Proceedings of the 13th International Conference on Fast Sea Transportation, FAST 2015, DC, USA, 2015.
[7] M. Diez, S. Volpi, A. Serani, F. Stern, E.F. Campana, Simulation-based design optimization by sequential multi-criterion adaptive sampling and dynamic radial basis functions. in advances in evolutionary and deterministic methods for design, Optim. Control Eng Sci. (2019) 213–228.
[8] A. Farkas, N. Degiuli, I. Martic, Numerical investigation into the interaction of resistance components for a series 60 catamaran, Ocean. Eng. 146 (2017) 151–169.
[9] J.H. Holland, Genetic algorithms and the optimal allocation of trials, SIAM J. Comp. 2 (2) (1973) 88–105.
[10] F. Huang, H. Kim, C. Yang, A new method for ship bulbous bow generation and modification, 24th International Ocean and Polar Engineering Conference, Busan, Korea, 2014.
[11] F. Huang, L. Wang, C. Yang, R. Royce, Hull form optimization of a TriSWACH for reduced drag, Proceedings of the Fast Sea Transport, Washington DC, USA, 2015.
[12] F. Huang, C. Yang, Hull form optimization of a cargo ship for reduced drag, J. Hydrodyn. 28 (2) (2016) 173–183.
[13] ITTC Specialist Committee, Recommended procedures and guidelines – uncertainty analysis in CFD verification and validation methodology and procedures, 25th International Towing Tank Conference, Fukuoka, 2011.
[14] D.R. Jones, M. Schonlau, W.J. Welch, Efficient global optimization of expensive black-box functions, J. Global Optim. 13 (4) (1998) 455–492.
[15] D. Karaboga, B. Basturk, A powerful and efficient algorithm for numerical function optimization: artificial bee colony (ABC) algorithm, J. Global Optim. 39 (3) (2007) 459–471.
[16] J. Kennedy, R. Eberhart, Particle swarm optimization, Proceedings of IEEE International Conference on Neural Networks, Perth, Australia, 1995.
[17] S.H. Kim, S.W. Na, Response surface method using vector projected sampling points, Struct. Saf. 19 (1) (1997) 3–19.
[18] C. Yang, Hydrodynamic optimization of multihull ships, Proceedings of the Fast Sea Transport, Honolulu, Hawaii, USA, 2011.
[19] J. Knowles, ParEGO: a hybrid algorithm with on-line landscape approximation for expensive multiobjective optimization problems, IEEE Trans. Evol. Comput. 10 (1) (2006) 50–66.
[20] X. Liu, M. Zhao, D.C. Wan, J. Wu, Hull form multi-objective optimization for a container ship with Neumann–Michell theory and approximation model, Int. J. Offshore Polar 27 (4) (2017) 423–432.
[21] F. Noblesse, F. Huang, C. Yang, The Neumann-Michell theory of ship waves, J. Eng. Math. 79 (1) (2013) 51–71.
[22] X. Qi, A. Miao, D.C. Wan, A Nurbs-based hull surface modification method for hydrodynamic optimization, 13th ISOPE Pacific/Asia Offshore Mechanics Symposium, Jeju, Korea, 2018.
[23] T.W. Sederberg, S.R. Parry, Free-form deformation of solid geometric models, ACM Siggraph Comput. Graph. 20 (4) (1986) 151–160.
[24] Z. Shen, D.C. Wan, An irregular wave generating approach based on naoe-FOAMSJTU solver, China Ocean. Eng. 30 (2016) 177–192.
[25] Z. Shen, D.C. Wan, P.M. Carrica, Dynamic overset grids in OpenFOAM with application to KCS self-propulsion and maneuvering, Ocean. Eng. 108 (2015) 287–306.
[26] T.W. Simpson, Comparison of Response Surface and Kriging models in the Multidisciplinary Design of an Aerospike Nozzle, Institute for Computer Applications in Science and Engineering, NASA Langley Research Centre, 1998.
[27] T.W. Simpson, T.M. Mauery, J.J. Korte, F. Mistree, Kriging models for global approximation in simulation-based multidisciplinary design optimization, AIAA J. 39 (12) (2001) 2233–2241.
[28] A. Souto-Iglesias, D. Fernandez-Gutierrez, L. Perez-Rojas, Experimental assessment of interference resistance for a Series 60 catamaran in free and fixed trim-sinkage conditions, Ocean. Eng. 53 (2012) 38–47.
[29] N. Srinivas, K. Deb, Multiobjective optimization using nondominated sorting in genetic algorithms, Evol. Comp. 2 (3) (1995) 221–248.
[30] Y. Tahara, M. Diez, S. Volpi, X. Chen, E.F. Campana, F. Stern, CFD-based multi-objective stochastic optimization of a waterjet propelled high speed ship, Proceedings of the 30th Symposium on Naval Hydrodynamics, Hobart, Tasmania, Australia, 2014.
[31] Y. Tahara, D. Peri, E.F. Campana, F. Stern, Computational fluid dynamics-based multiobjective optimization of a surface combatant using a global optimization method, J. Mar. Sci. Technol. 13 (2) (2008) 95–116.
[32] Y. Tahara, D. Peri, E.F. Campana, F. Stern, Single-and multi-objective design optimization of a fast multihull ship: numerical and experimental results, J. Mar. Sci. Technol. 16 (4) (2011) 412–433.
[33] J. Wang, W. Zhao, D.C. Wan, Free maneuvering simulation of ONR Tumblehome using overset grid method in naoe-foam-SJTU solver, Proceedings of the 31th Symposium on Naval Hydrodynamics, Monterey, USA, 2016.
[34] J. Wang, L. Zou, D.C. Wan, CFD simulations of free running ship under course

keeping control, Ocean. Eng. 141 (2017) 450–464.
[35] L. Wang, F. Huang, C. Yang, Grid generation on Nurbs surfaces developed for ship hull form optimization, 24th International Ocean and Polar Engineering Conference, Busan, Korea, 2014.
[36] J. Wu, X. Liu, M. Zhao, D.C. Wan, Neumann-Michell theory-based multi-objective optimization of hull form for a naval surface combatant, Appl. Ocean. Res. 63 (2017) 129–141.
[37] C. Yang, F. Huang, An overview of simulation-based hydrodynamic design of ship hull forms, J. Hydrodyn. 28 (6) (2016) 947–960.
[38] C. Yang, H. Kim, F. Huang, Hydrodynamic optimization of a triswach, J. Hydrodyn. 26 (6) (2015) 856–864.
[39] R. Zha, H. Ye, Z. Shen, D.C. Wan, Numerical computations of resistance of high speed catamaran in calm water, J. Hydrodyn. 26 (6) (2014) 930–938.
[40] B. Zhang, Research on optimization of hull lines for minimum resistance based on Rankine source method, J. Mar. Sci. Technol. 20 (1) (2012) 89–94.
[41] C.L. Zhang, J.B. Wang, Y. Zhu, F. Noblesse, Stationary phase and practical numerical evaluation of ship waves in shallow water, J. Hydrodyn. 29 (5) (2017) 817–824.